

The effect of galaxy mass ratio on merger–driven starbursts

T. J. Cox^{1*}, Patrik Jonsson², Rachel S. Somerville³, Joel R. Primack², and Avishai Dekel⁴

¹*Harvard-Smithsonian Center for Astrophysics, 60 Garden St., Cambridge, MA 02138, USA*

²*Department of Physics, University of California, Santa Cruz, 1156 High St., Santa Cruz, CA 95064, USA*

³*Max-Planck-Institut für Astronomie, Königstuhl 17, D-69117 Heidelberg, Germany*

⁴*Racah Institute of Physics, The Hebrew University, Jerusalem, 91904, Israel*

2 February 2008

ABSTRACT

We employ numerical simulations of galaxy mergers to explore the effect of galaxy mass ratio on merger–driven starbursts. Our numerical simulations include radiative cooling of gas, star formation, and stellar feedback to follow the interaction and merger of four disk galaxies. The galaxy models span a factor of 23 in total mass and are designed to be representative of typical galaxies in the local Universe. We find that the merger–driven star formation is a strong function of merger mass ratio, with very little, if any, induced star formation for large mass ratio mergers. We define a burst efficiency that is useful to characterize the merger–driven star formation and test that it is insensitive to uncertainties in the feedback parameterization. In accord with previous work we find that the burst efficiency depends on the structure of the primary galaxy. In particular, the presence of a massive stellar bulge stabilizes the disk and suppresses merger–driven star formation for large mass ratio mergers. Direct, co–planar merging orbits produce the largest tidal disturbance and yield that most intense burst of star formation. Contrary to naive expectations, a more compact distribution of gas or an increased gas fraction both decrease the burst efficiency. Owing to the efficient feedback model and the newer version of SPH employed here, the burst efficiencies of the mergers presented here are smaller than in previous studies.

Key words: galaxies: interactions – galaxies: evolution – galaxies: starburst – galaxies: formation – methods: numerical.

1 INTRODUCTION

While mergers between galaxies of approximately equal mass, so called major mergers, garner a significant amount of observational and theoretical interest, it is likely that galaxies accreting much smaller objects are also important drivers of galaxy evolution. This possibility is a natural consequence of the hierarchical growth of structure predicted by the Lambda cold dark matter (Λ CDM; a.k.a., “Double Dark”) cosmology (see, e.g., Somerville et al. 2001). In this scenario every dark matter halo, and presumably the galaxy it hosts, is assembled through a continuous and varied merger history comprised of *many* small accretion events and a *few* “major” ones (see, e.g., Lacey & Cole 1993; Wechsler et al. 2002).

The transformation of galactic systems by major mergers has been well studied. Numerical simulations demonstrate that major mergers between spiral galaxies produce remnants that generally resemble elliptical galaxies,

whose shapes are determined by random motions, i.e., they are pressure-supported, and which possess projected mass distributions that scale approximately as $\sim r^{1/4}$ (e.g., Barnes & Hernquist 1991, 1992; Hernquist 1992, 1993b; Naab & Burkert 2003; Cox et al. 2006,?). Observations of fine structure, kinematic subsystems, the bimodal distributions of global clusters in elliptical galaxies, and the light profiles of merger remnants lend support to the assertion that elliptical galaxies are the byproduct of major galaxy mergers – in what is commonly termed the “merger hypothesis” (Toomre 1977). For further information regarding the observational and theoretical evidence supporting the merger hypothesis, or the general dynamics of galaxy interactions, we refer the interested reader to reviews by Barnes & Hernquist (1992), Schweizer (1998), and Struck (2006).

While major mergers are likely to be the most dramatic events in a galaxy’s assembly history, it is likely that the more prevalent minor mergers give rise to the wide variety of galaxy morphology that defines many classification systems (Hubble 1926; de Vaucouleurs 1977; van den Bergh

* E-mail: tcx@cfa.harvard.edu

1960; Sandage 1975). The morphological transformation owing to the effects of minor merger has been studied via numerous numerical simulations, which demonstrate that galactic disks become warped and heated as a result of the accretion of a satellite (Quinn & Goodman 1986; Toth & Ostriker 1992; Quinn et al. 1993; Walker et al. 1996; Huang & Carlberg 1997; Velazquez & White 1999; Font et al. 2001), that the satellite itself is tidally stripped to produce stellar streams throughout the galactic halo (Johnston et al. 1999; Helmi & White 2001; Mayer et al. 2002; Boylan-Kolchin & Ma 2007), and that the remnant galaxy will be a systematically earlier Hubble type (Aguerre et al. 2001; Naab & Burkert 2003; Bournaud et al. 2004, 2005; Eliche-Moral et al. 2006; Maller et al. 2006). Furthermore, there is an increasing amount of evidence that these theoretical expectations are consistent with observations in the local universe (e.g., Ibata et al. 2001; Dalcanton & Bernstein 2002; Navarro et al. 2004; Bullock & Johnston 2005).

While both major and minor mergers are expected to produce some degree of morphological evolution, it is still unclear whether all mergers will lead to a merger-driven starburst and therefore drive spectrophotometric evolution. There is mounting evidence that near equal mass (major) mergers trigger the most vigorous star-forming galaxies in the local Universe, the ultraluminous infrared galaxies (ULIRGs) with bolometric luminosities greater $10^{12} L_{\odot}$ (see, e.g., Sanders & Mirabel 1996; Borne et al. 2000). More generally, large statistical samples consistently indicate a clear anticorrelation between projected galaxy pair separation and star formation indicators in the optical (Barton et al. 2000; Nikolic et al. 2004; Lambas et al. 2003; Sol Alonso et al. 2006; Barton et al. 2007; Ellison et al. 2007) and the infrared (Geller et al. 2006; Smith et al. 2007). Moreover, numerical simulations naturally explain these observations as centrally concentrated starbursts triggered by tidal forces that attend the galaxy interaction (see, e.g., Barnes & Hernquist 1991; Mihos & Hernquist 1994b, 1996; Springel 2000; Kapferer et al. 2005; Cox et al. 2006; di Matteo et al. 2007).

In contrast, relatively little is known about the resulting starbursts during interactions between galaxies of unequal mass. Observationally, statistical studies are hampered by magnitude limits and confusion with background sources, but preliminarily indicate that enhanced star formation (as measured by $H\alpha$) is strongly dependent upon the relative mass (or magnitude) of the interacting galaxies. Initial results using the CfA2 Redshift Survey indicated no correlation between galaxy pair separation and equivalent width of $H\alpha$ (Woods et al. 2006), suggesting that minor mergers do not lead to merger-driven star formation. More recent studies using the Sloan Digital Sky Survey (SDSS, Ellison et al. 2007; Woods & Geller 2007) find that minor mergers indeed lead to enhanced star formation, however the data also suggest that the enhancement is primarily observed in the satellite galaxy while the larger primary galaxy has star forming properties similar to non-interacting field galaxies (Woods & Geller 2007). More locally, detailed observations of individual galaxies in the nearby Universe suggest that minor mergers may be responsible for some degree of star formation enhancement, e.g., NGC 278 (Knapen et al. 2004), NGC 3310 (Smith et al. 1996),

NGC 4064 and NGC 4424 (Cortés et al. 2006), NGC 7742 (Mazzuca et al. 2006), and the M81 group (Walter et al. 2002; Förster Schreiber et al. 2003).

While numerical simulations have been used extensively in the study of star formation in major mergers, there exist only a handful of previous simulations that have specifically quantified the star formation history of unequal mass galaxy mergers. These works have established that tidal perturbations can induce bar formation, inflows of gas, and subsequent bursts of star formation when the primary disks are susceptible to instabilities, such as when they do not contain a stellar bulge (Hernquist 1989; Mihos & Hernquist 1994a; Hernquist & Mihos 1995). However, because these studies performed only a limited number of simulations, and did not include some important physical processes, our understanding of the relationship between mergers of unequal mass galaxies and the resulting star formation is still highly incomplete.

In this paper we fill in this gap by describing a large set of numerical simulations of unequal mass disk-galaxy mergers. In particular, we seek to extend and improve the pioneering work of Mihos & Hernquist (1994a) and provide a more complete picture of merger-driven star formation, including its dependence upon the merging orbit and the structure of the primary galaxy. We will also take advantage of recent improvements in the treatment of supernovae feedback (Springel 2000; Springel & Hernquist 2003; Cox et al. 2006) and smoothed-particle hydrodynamics (SPH) methodology (Springel & Hernquist 2002) which allow us to follow the evolution of galaxies with larger gas fraction than was possible previously.

The results of our simulations are relevant for a number of related studies. Many models of galaxy formation often employ merger-driven star formation as a necessary ingredient to produce bright galaxies throughout cosmic time (Guiderdoni et al. 1998; Somerville et al. 2001; Baugh et al. 2005). Our results will serve as a useful input to such models. In addition, our models will be a valuable tool for interpreting observations. By comparison to the observed star formation in pairs of galaxies (Barton et al. 2000; Woods et al. 2006; Woods & Geller 2007; Lin et al. 2007), we can constrain our models and infer the contribution of mergers to the universal star formation rate. The numerical models have also been used to generate “simulated observations” of the merging galaxies through radiative transfer modeling (Jonsson 2004; Jonsson et al. 2006; Jonsson 2006), to study dust attenuation in spiral galaxies (Rocha et al. 2007), to understand the size, shape, and scaling relations of merger remnants (Dekel & Cox 2006; Novak et al. 2006; Covington et al. 2007), and to calibrate non-parametric indicators of galaxy morphology (Lotz et al., in preparation), which can then be used to quantify the merger rate over cosmic time.

We organize this paper as follows: Our numerical techniques are summarized in §2 and the galaxy models used for our galaxy interactions are described in §3. A general description of the mergers is provided in §4, including a discussion about the possible methods to quantify the merger-driven star formation. Some additional models are explored in §5. Finally, we discuss our results and conclude in §6.

2 NUMERICAL SIMULATIONS

All of the numerical simulations performed in this work use the N-Body/SPH code GADGET (Springel et al. 2001). In general, our methodology is similar to Cox (2004) and Cox et al. (2006), and thus, in this section we will only review selected aspects of our techniques and methodology that are relevant to this work. We use the first version of GADGET, however the smoothed particle hydrodynamics (SPH) modules are upgraded (with the aid of V. Springel) to use the “conservative entropy” version that is detailed in Springel & Hernquist (2002). The radiative cooling rate $\Lambda_{\text{net}}(\rho, u)$ is computed for a primordial plasma as described in Katz et al. (1996). Stars are formed at a rate determined by the local SPH density normalized to match observed star formation rates (Kennicutt 1998). Furthermore, we employ a threshold density ρ_{th} , below which stars do not form. Finally, star formation occurs within individual SPH particles and each particle can stochastically spawn two stellar particles.

One of the largest uncertainties associated with current numerical simulations including star formation is the implementation of supernova feedback. Because of the limited resolution achievable in state-of-the-art numerical simulations, most work performed to date adopts a “sub-grid” approach where the physical processes associated with feedback are included in a simple, yet flexible manner with free parameters that can be tuned to match observations. Unfortunately, there are often a range of acceptable free parameters which produce distinct star formation histories or remnant morphologies (see, e.g., Thacker & Couchman 2000; Kay et al. 2002; Springel et al. 2005b; Cox et al. 2006). For many of the simulations performed in this work, we have run two different feedback models, either the *n0med* or *n2med* models as introduced in Cox et al. (2006). Both models are termed “medium” because they dissipate feedback energy on a 8 Myr timescale. The *n2med* model treats star-forming gas with a stiff equation of state while *n0med* assumes this gas is isothermal with an effective temperature $\sim 10^5$ K. We will compare these two feedback models in §4.3.2 in order to determine how these assumptions influence the resulting star-formation history.

All simulations presented throughout this work use a gravitational softening length of 0.1 kpc for all baryonic particles, and 0.4 kpc for dark matter particles. The SPH smoothing length is required to be greater than half the gravitational softening length, or > 50 pc. We have performed a few tests with both smaller and larger softening lengths and found little or no differences in the star-formation history, suggesting that we have achieved numerical convergence (see Cox et al. 2006, for similar tests).

3 GALAXY MODELS

Because our primary motivation is to investigate collisions between unequal mass galaxies, we wish to construct galaxies with a range of different masses. Furthermore, because the properties of galactic disks depend on mass, we also need to design galaxy models that are physically plausible. To begin, we select the largest galaxy model to have a total stellar mass of $M_{\star} \sim 5.0 \times 10^{10} M_{\odot}$, slightly above the transitional mass of $3.0 \times 10^{10} M_{\odot}$ found to divide large galaxies

with old stellar populations from smaller star forming ones (Kauffmann et al. 2003). Three smaller galaxy models are included that have M_{\star} equal to $1.5 \times 10^{10} M_{\odot}$, $0.5 \times 10^{10} M_{\odot}$ and $0.1 \times 10^{10} M_{\odot}$, making the total stellar mass span a range of 50. We label the largest of these models G3, and the rest G2, G1, and, finally, the smallest G0.

Once the stellar masses are fixed, we next determine the stellar size using the late-type galaxy size-mass relationship found by Shen et al. (2003, eq. 18), from the analysis of 140,000 galaxies in the Sloan Digital Sky Survey. This relation fixes the half-light radius R_{50} for each model, which we assume is equivalent to the stellar half-mass radius.

Because each model is assumed to be a late-type galaxy, they consist of a stellar and gaseous exponential disk, a stellar Hernquist (1990) bulge, all embedded in a dark matter halo. A general description of the methods employed to construct model disk galaxies, including the assumed profiles, can be found in Cox et al. (2006), however, those models are not identical to the ones used here. The model parameters used for this work, which are listed in Table 1, are selected such that each model galaxy is statistically average, as opposed to Cox et al. (2006) who specifically modeled a gas-rich Sbc galaxy.

To ensure that the models are statistically average, the mass of the stellar disk and bulge are constrained by the half-mass radius R_{50} and the observed bulge-to-disk ratio of local late-type galaxies (de Jong 1996). To quantify the latter constraint, we assume a K-band mass-to-light ratio of 0.7 and 0.5 for the bulge and disk, respectively, and fit a line to the de Jong (1996) data, finding

$$\log(M_{\text{bulge}}) = 1.6 \log(M_{\text{disk}}) - 1.03, \quad (1)$$

where the masses are in units of $10^{10} M_{\odot}$. Using this formula, along with the fixed total stellar mass for each model, both the stellar bulge and stellar disk masses are determined. To determine the size of these components (the exponential disk scale radius R_d and the bulge scale radius R_b) an iterative approach is used where the first step is to guess an initial disk scale radius R_d . The bulge scale radius R_b is then fixed by the empirical correlation between disk and bulge sizes found by de Jong (1996, see his Eq. 5). This initial guess for the disk and bulge mass distributions is then compared to the desired half-mass radius R_{50} and corrected until the two are within 1% of each other.

In addition to the stellar component, each galaxy model contains gas, the fuel for star formation. Motivated by observations of local late-type galaxies (e.g., Broeils & van Woerden 1994), gas is distributed in an extended exponential disk with a scale radius proportional to that of the stellar disk, $r_{\text{gas}} = \alpha r_{\text{star}}$. In our default model we assume $\alpha = 3$. To determine the mass of gas, we use the observed trend that systems with lower total/stellar mass have a higher gas fraction (Bell et al. 2003; Geha et al. 2006). Using data from Bell et al. (2003, kindly provided in electronic form by E. Bell), we parameterize this relationship as

$$\log(M_{\text{gas}}) = 0.78 \log(M_{\star}) + 1.74, \quad (2)$$

where both masses are in units of $10^{10} M_{\odot}$. Because this relation is derived from the mean gas content as a function of total baryonic mass, the model disks will contain only moderate quantities of gas, and are therefore unlikely to produce large bursts of star formation. In §5.4 we will perform a small

Table 1. Properties of galaxy models used in this study. The compound galaxy has a total mass M_{vir} , and is composed of dark matter and a stellar disk, stellar bulge, and gaseous disk. The total mass of each baryonic component and their mass fractions are provided. The dark halo has an NFW profile with concentration c and spin parameter λ . The stellar disk has a total mass M_{disk} which is a fraction m_d of the total mass and a fraction j_d of the total angular momentum. The disk has an exponential profile of scale radius R_d and scale height z_0 . Each galaxy model contains a spherical bulge of mass M_{bulge} and mass fraction m_b , with an exponential profile of scale length R_b and zero angular momentum. The gas mass is M_{gas} , a fraction m_g of the total mass, and j_g is the angular momentum fraction. The gas disk, like its stellar companion, is assumed to have an exponential surface density with a scale radius α times R_d . We define the gas fraction f as the fraction of the *total* disk mass which is gaseous. Finally, each system is represented by N particles, which represent the dark matter, stellar disk, bulge and gaseous galaxy.

	G3	G2	G1	G0
M_{\star} ($10^{10} M_{\odot}$)	5.0	1.5	0.5	0.1
R_{50} (kpc)	3.86	2.88	2.35	1.83
Total Mass, M_{vir} ($10^{10} M_{\odot}$)	116.0	51.0	20.0	5.0
Concentration, $c=R_{\text{vir}}/r_s$	6	9	12	14
Spin Parameter, λ	0.05	0.05	0.05	0.05
Disk Mass, M_{disk} ($10^{10} M_{\odot}$)	4.11	1.35	0.47	0.098
Disk Mass Fraction, m_d	0.035	0.026	0.024	0.019
Disk Scale Length, R_d (kpc)	2.85	1.91	1.48	1.12
Disk Scale Height, z_0 (kpc)	0.40	0.38	0.30	0.22
Disk Spin Fraction, j_d	0.015	0.010	0.010	0.010
Bulge Mass, M_{bulge} ($10^9 M_{\odot}$)	8.9	1.5	0.3	0.02
Bulge-to-disk ratio, B/D	0.22	0.11	0.06	0.02
Bulge Mass Fraction, m_b	0.008	0.003	0.002	<0.001
Bulge Radial Scale Length, R_b (kpc)	0.37	0.26	0.20	0.15
Gas Mass, M_{gas} ($10^{10} M_{\odot}$)	1.22	0.48	0.20	0.06
Gas Mass Fraction, m_g	0.011	0.009	0.010	0.012
Gas Fraction, f	0.196	0.242	0.286	0.375
Gas Scale Multiplier, α	3.0	3.0	3.0	3.0
Gas Spin Fraction, j_g	0.012	0.010	0.013	0.019
N	240,000	150,000	95,000	51,000
N_{dm}	120,000	80,000	50,000	30,000
N_{gas}	50,000	30,000	20,000	10,000
N_{disk}	50,000	30,000	20,000	10,000
N_{bulge}	10,000	10,000	5,000	1,000

number of additional mergers using galaxies with higher gas fractions.

The final component of the galactic system is the massive dark-matter halo. Each model contains a dark halo with a Navarro et al. (1996, NFW) profile whose properties are selected so that the rotation curve satisfies the baryonic Tully-Fisher relation (Bell & de Jong 2001; Bell et al. 2003). Because most of the models require very little non-baryonic mass in order to satisfy the Tully-Fisher relation, we do not include adiabatic contraction. Still, the resultant halo concentrations c are below the mean found in cosmological N-body simulations (Bullock et al. 2001), a tension that has been emphasized previously (see, e.g., Alam et al. 2002). We note that (motivated by observations) the galaxy models have systematically higher baryon fractions in higher mass galaxies, resulting in a total mass ratio 23 between G3 and G0 as opposed to a ratio of 50 in stellar mass.

The construction of these galaxy models is based upon Hernquist (1993a) and its more recent incarnation to include a NFW halo (Springel & White 1999; Springel 2000). We note that because the spatial distribution of baryons is fixed by the galaxy model, the halo spin does not determine the size of the gaseous and stellar disk, as in many popular

models for disk formation (see, e.g., Mo et al. 1998). However, we feel that our procedure is adequate since it produces stable disks, provided that the velocity dispersion of the disks is chosen such that the Toomre stability parameter Q is greater than 1 at all radii and the feedback model can provide adequate pressure support to the gas.

3.1 Evolution of Isolated Systems

The stability of our model galaxies is demonstrated in Figure 1, which shows the projected gas and stellar surface densities after being evolved in isolation for ~ 1 Gyr (greater than 5 orbital periods in all models). While the mass distributions of each component are stable during the entire period that they are simulated, the noisy potential resulting from the finite particle number seeds transient instabilities (see Hernquist 1993a). These instabilities are most prominent in the G3 and G2 galaxies, which have larger disk surface densities than the less massive galaxy models.

The stability of the galaxy models is also reflected by a constant star-formation rate (SFR), regardless of the feedback model employed, as shown in Figure 2. The average SFR is 0.95, 0.25, 0.06 and 0.001 $M_{\odot} \text{ yr}^{-1}$ for models G3,

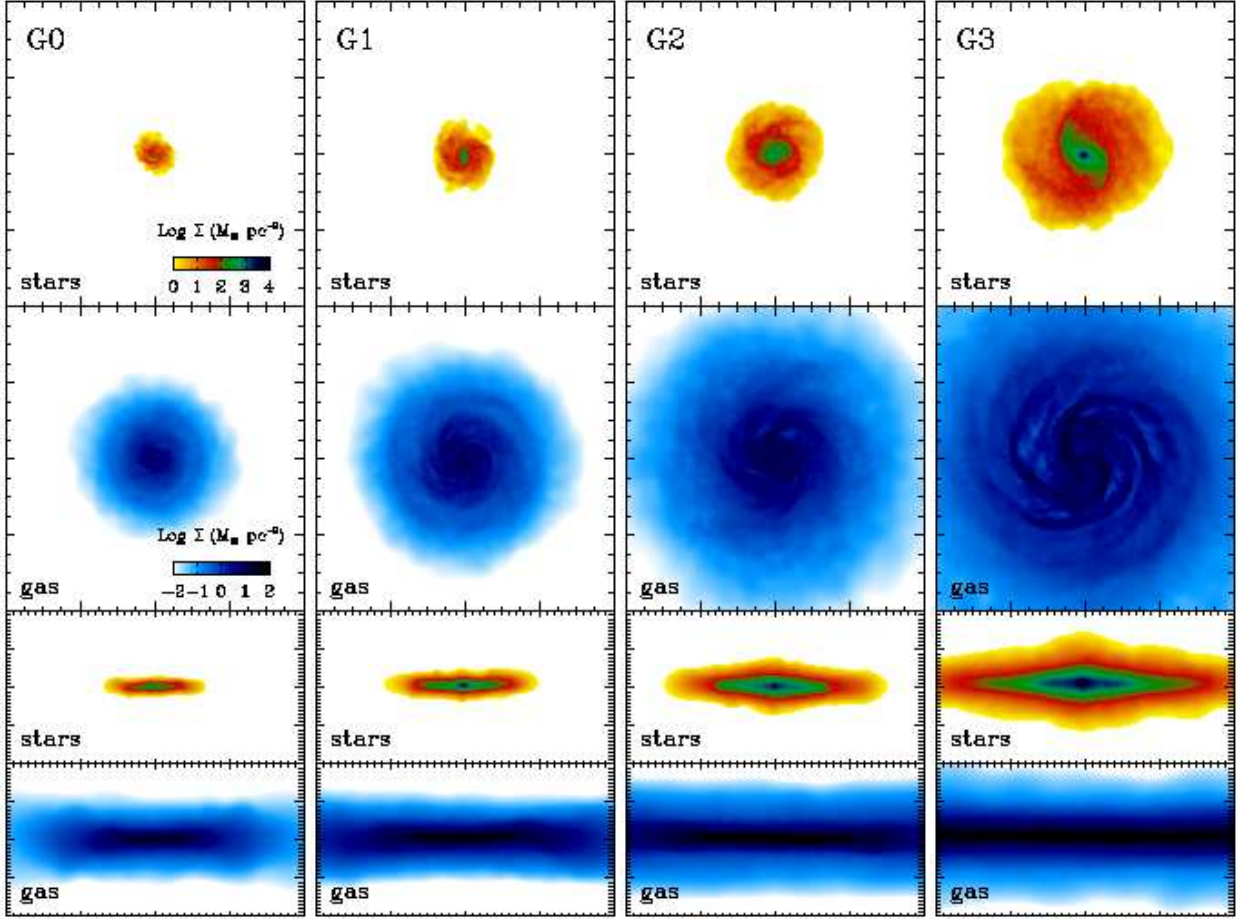


Figure 1. Projected mass density for each galaxy model, G0 (left column), G1, G2, and G3 (right column) when simulated in isolation for ~ 1 Gyr, which is greater than 5 orbital periods at the half-mass radius in all models. Each row shows the projected stellar or gaseous mass as specified in the lower-left of each panel. The top two rows show the galaxies face-on, while the bottom two rows show the edge-on view. Each panel measures 80 kpc on a side. A color bar in the upper-left panel indicates the stellar surface density scale that is used for all panels, and the color bar in the one below indicates the gaseous surface density scale that is used in all panels.

G2, G1, and G0, respectively, during the 1 Gyr period shown in Figure 2. The average SFR scales as $M_{\text{gas}}^{3/2}$, as is expected from our Schmidt-type star-formation law (see Cox et al. 2006). The SFR of the smaller galaxies, G1 and G0, display increased fluctuations owing to the more significant impact of feedback, decreasing resolution, and the fixed star-formation threshold density ρ_{th} . The SFRs shown in Figure 2 are constant for ~ 2 Gyr. After this, galaxies G3 and G2 begin to consume a significant fraction of their high-density ($> \rho_{\text{th}}$) gas and their SFR eventually drops to approximately one-tenth its initial value at 6 Gyr. Another consequence of the adopted star-formation law is that the star-formation timescale scales with gas density, viz., $\tau_{\text{SF}} \approx M_{\text{gas}}/\text{SFR} \sim \rho^{-1/2}$, in other words, more massive galaxies, with higher gas densities, have shorter gas consumption timescales. As a result, the more massive galaxy models consume a larger fraction of their initial gas mass than the smaller ones. During the entire 6 Gyr evolution, model G3 converts 26% of its original gas to stars, G2 converts 22%, G1 converts 11%, and G0 converts 3%.

4 GALAXY MERGERS

The previous section defined four galaxy models G3-G0 and established the stability of these models by simulating them in isolation. In this section we discuss the outcome of binary mergers between these models on a single merging orbit. Performing a single merger between all combinations of the four models yields four equal-mass major mergers and six unequal-mass mergers. In the following section (§5), we discuss a number of additional merger simulations to determine systematic dependencies.

4.1 Fiducial Encounters

For reference, we list the merger mass ratios in Table 2. Mass ratios are given for the total, stellar and baryonic masses. In what follows we will label a simulated mergers by its two merging constituents. For example, G3G1 is a merger between our largest galaxy G3 and the second-smallest G1. The total mass ratio is 5.8 to 1, i.e., model G1 is 5.8 times smaller than G3. When referring to the interacting galaxies, the less massive galaxy will be termed the satellite and the more massive galaxy the primary. We note that some galaxy

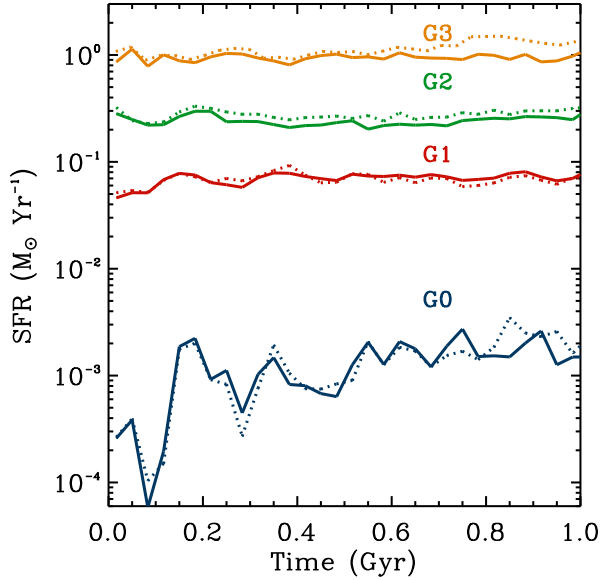


Figure 2. Star formation for our isolated galaxy models G3, G2, G1 and G0. Each model has been run with two separate feedback models and both star-formation histories are shown, *n0med* with a dotted line and *n2med* with a solid line.

Table 2. Total, stellar, and baryonic mass ratios between our four galaxy models G3, G2, G1, and G0.

Primary	Satellite	Total	Stellar	Baryonic
G3	G3	1:1	1:1	1:1
G3	G2	2.3:1	3.3:1	3.1:1
G3	G1	5.8:1	10.0:1	8.9:1
G3	G0	22.7:1	50.0:1	38.9:1
G2	G2	1:1	1:1	1:1
G2	G1	2.6:1	3.0:1	2.8:1
G2	G0	10.0:1	15.0:1	12.4:1
G1	G1	1:1	1:1	1:1
G1	G0	3.9:1	5.0:1	4.4:1
G0	G0	1:1	1:1	1:1

models (G2, G1, and G0) can be a primary in one interaction and a satellite in another.

All galaxy interactions are initialized with a nearly unbound elliptical orbit with eccentricity $\epsilon = 0.95$. The initial separation is fixed to be slightly less than the virial radius of the primary and is 250, 100, 80, and 50 kpc for G3, G2, G1, and G0 models, respectively. The pericentric distance is set to be 13.6, 3.8, 2.96, and 2.24 when the primary is G3, G2, G1, and G0, respectively. The resulting interactions are fast and nearly radial, consistent with orbits found for dark matter halos in cosmological simulations (Vitvitska et al. 2002; Khochfar & Burkert 2006; Benson 2005; Zentner et al. 2005). The only exception to the above orbits is the merger G3G0, where the total mass ratio is 22.7 to 1, the largest mass ratio we simulate. In this case, the fiducial interaction was still not fully merged after the system was evolved for ~ 12 Gyr. In order to better compare this interaction with

the other, more rapid, mergers, we multiplied the initial velocity of the satellite by 0.2 so that the merger occurred during the 6 Gyr we followed each interaction.

Finally, the fiducial series of orbits are all prograde, i.e., the angular momentum of the orbit is (nearly) aligned with the spin of the primary. A slight tilt of 30° is introduced such that the interaction is not entirely co-planar. In section 5.1 we resimulate the G3G2 and G3G1 mergers with a variety of orbits to determine the dependence of merger-driven star formation on orbital angular momentum (R_{peri}) and merger alignment.

4.2 Merger Evolution

The evolution of a typical merger event is shown in Figures 3 and 4 for the G3G2 merger, and Figures 5 and 6 for the G3G1 merger. In both cases, the projected stellar surface density is first shown, followed by the projected gaseous surface density. The images shown in these figures are typical of the remaining mergers that are not shown, and are also consistent with what has been discussed in studies of equal mass mergers (e.g., Barnes & Hernquist 1991; Mihos & Hernquist 1996; Springel 2000; Cox et al. 2006), and unequal mass mergers (e.g., Hernquist 1989; Hernquist & Mihos 1995). For completeness, the following provides a brief outline of the merger process, and the resulting star formation.

In both of the mergers shown the satellite galaxy (G2 and G1) first makes a fast, direct approach toward the primary galaxy (G3). This close passage tidally distorts the disks and generates symmetric tails in both. Owing to the energetic orbit, the satellite separates again for several orbital periods (≥ 1 Gyr) before returning for its second encounter with the disk of the primary. A generic feature of all the interactions simulated here is the efficient loss of angular momentum by the satellite. In particular, even for large mass ratio encounters the orbits become almost entirely radial after the first or second close passage.

The loss of orbital angular momentum and eventual radial nature of the final merger limits the coupling between orbital and spin angular momentum, and therefore the tidal response. Most of the induced star formation during the final coalescence is a result of the collisional nature of the gas and the rapid fluctuations in the potential as the satellite oscillates through the center and the system finally relaxes. The collisional nature of the gas also produces several other features distinct from the stellar disk. During the first close passage, the satellite creates a snow-plow effect, as it clears out gas from the primary’s extended gas disk. This effect continues during each close passage until eventually the majority of the gas in the satellite has been stripped off, leaving a predominantly stellar satellite. However, by this point the orbit has decreased such that it is difficult to disentangle the two galaxies.

While it is beyond the scope of the current paper to provide a detailed analysis of the structure of the merger remnants, there are several qualitative features present in Figures 3–6 that motivate future inquiry. First, it is evident that the stellar disks have been thickened and dynamically heated during the accretion event, consistent with a number of previous numerical studies (e.g., Quinn & Goodman 1986; Quinn et al. 1993; Toth & Ostriker 1992; Walker et al. 1996; Velazquez & White 1999; Benson et al. 2004;

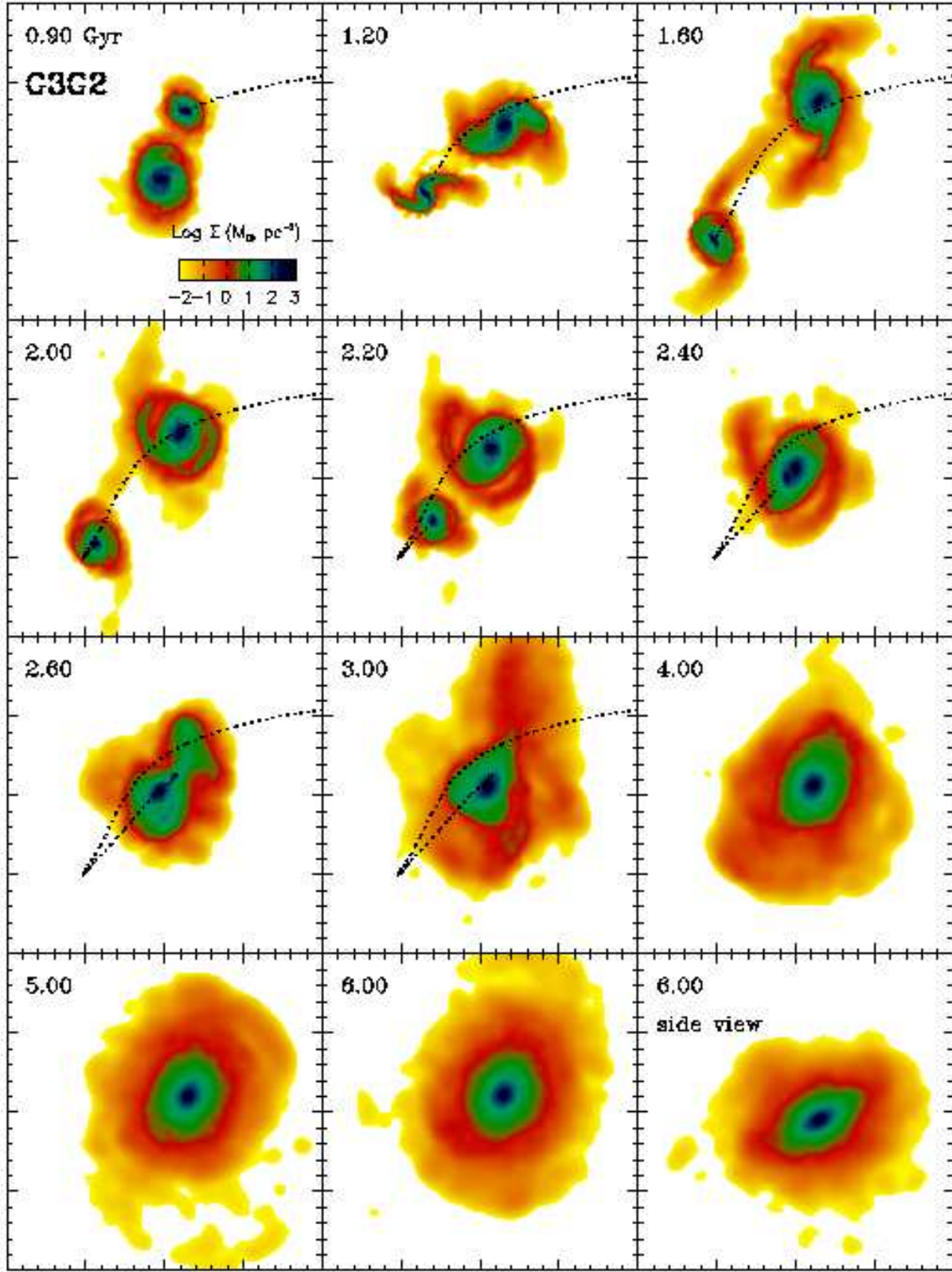


Figure 3. Projected stellar mass density during the G3G2 merger simulation as viewed in the orbital plane. Each panel measures 200 kpc on a side and the time, in Gyr, is displayed in the upper left of each panel. The orbit of the satellite galaxy G2 is denoted by a dotted line until it has completely merged with the primary galaxy. The bottom-right panel shows a side view of the final merger remnant, and clearly indicates the initial 30° inclination of the progenitor disk. The top-left panel indicates the color scale used in all panels.

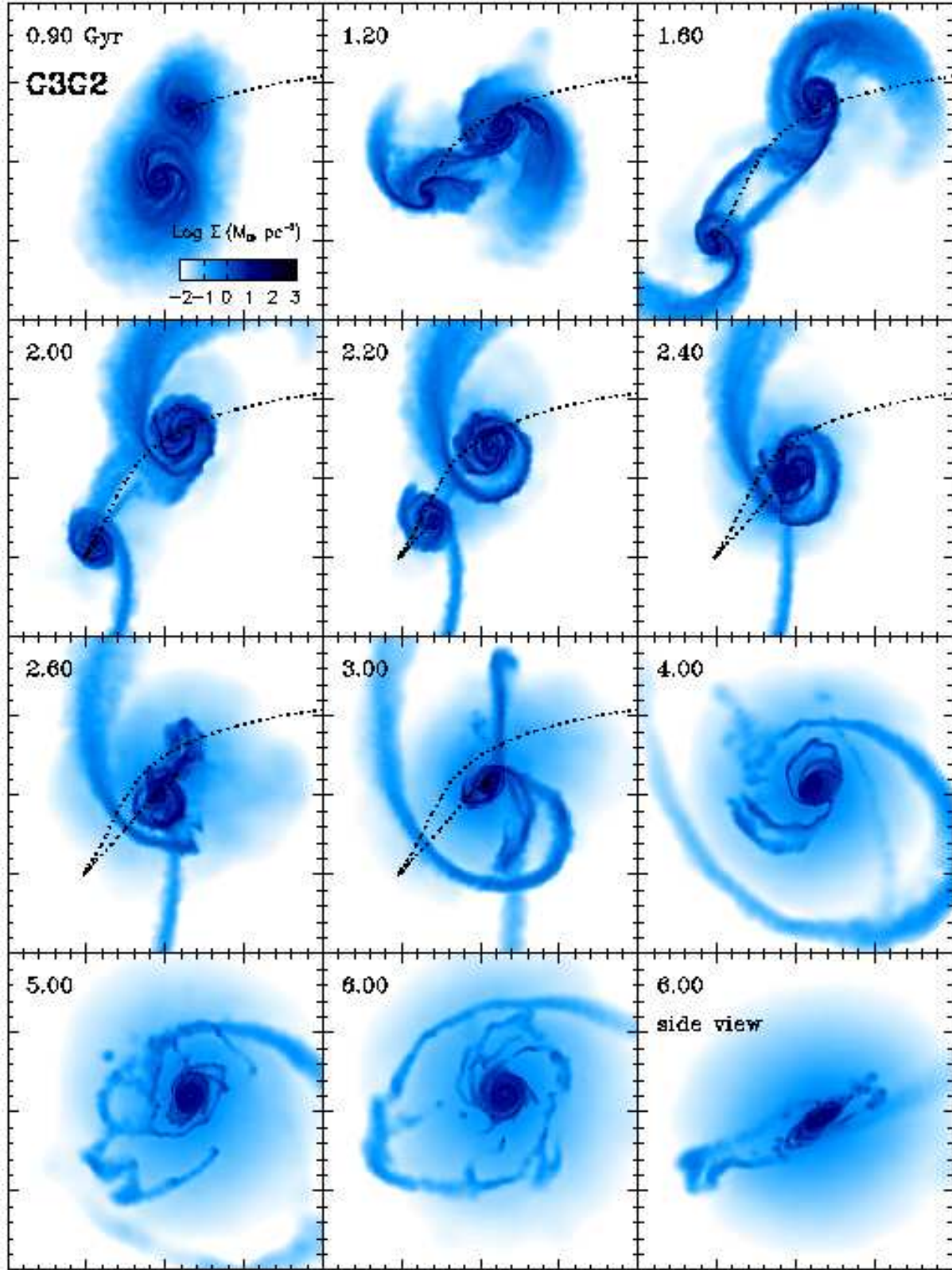


Figure 4. Similar to Figure 3, but for the gaseous component.

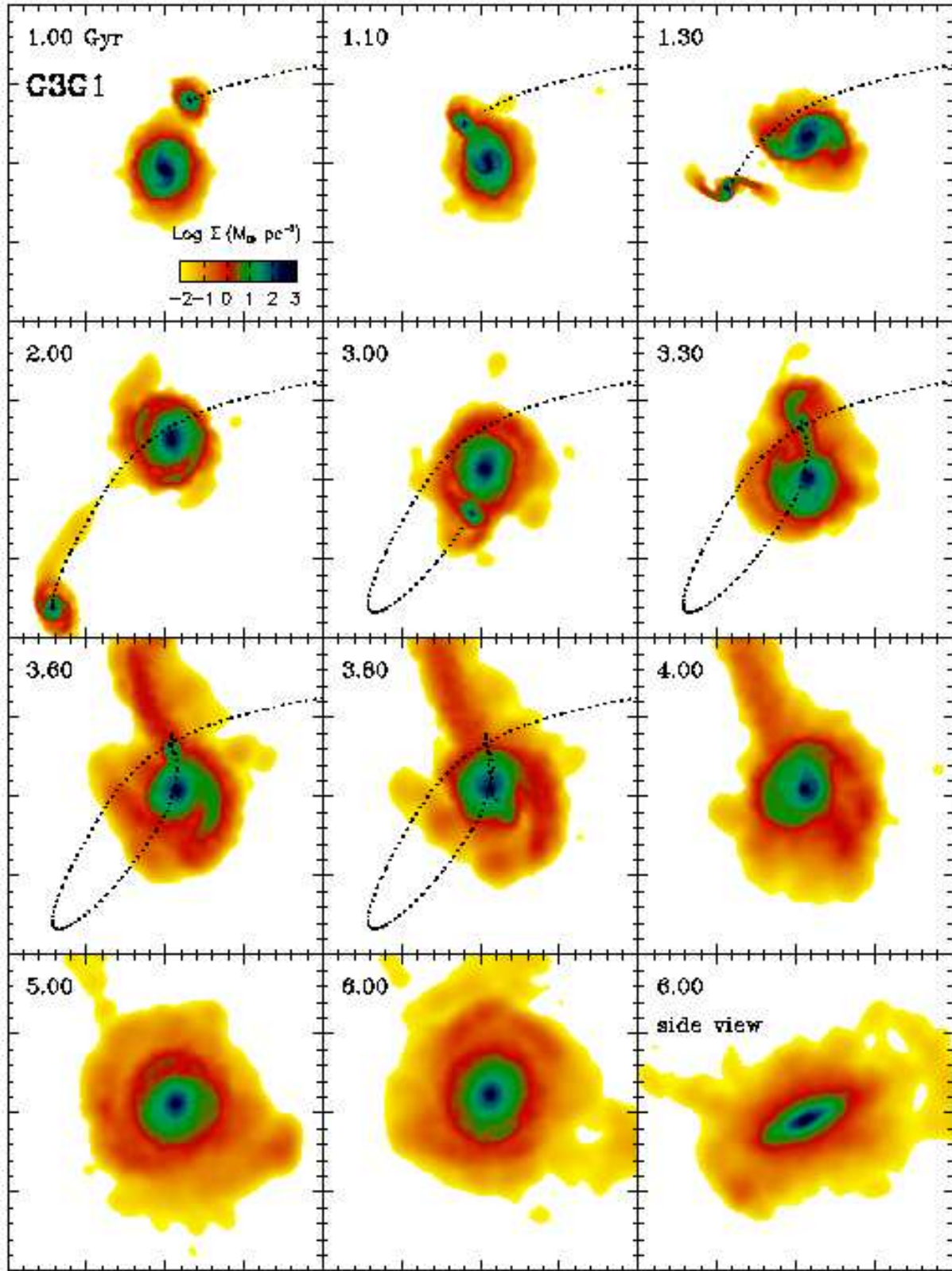


Figure 5. Similar to Figure 3, but the G3G1 merger is now shown.

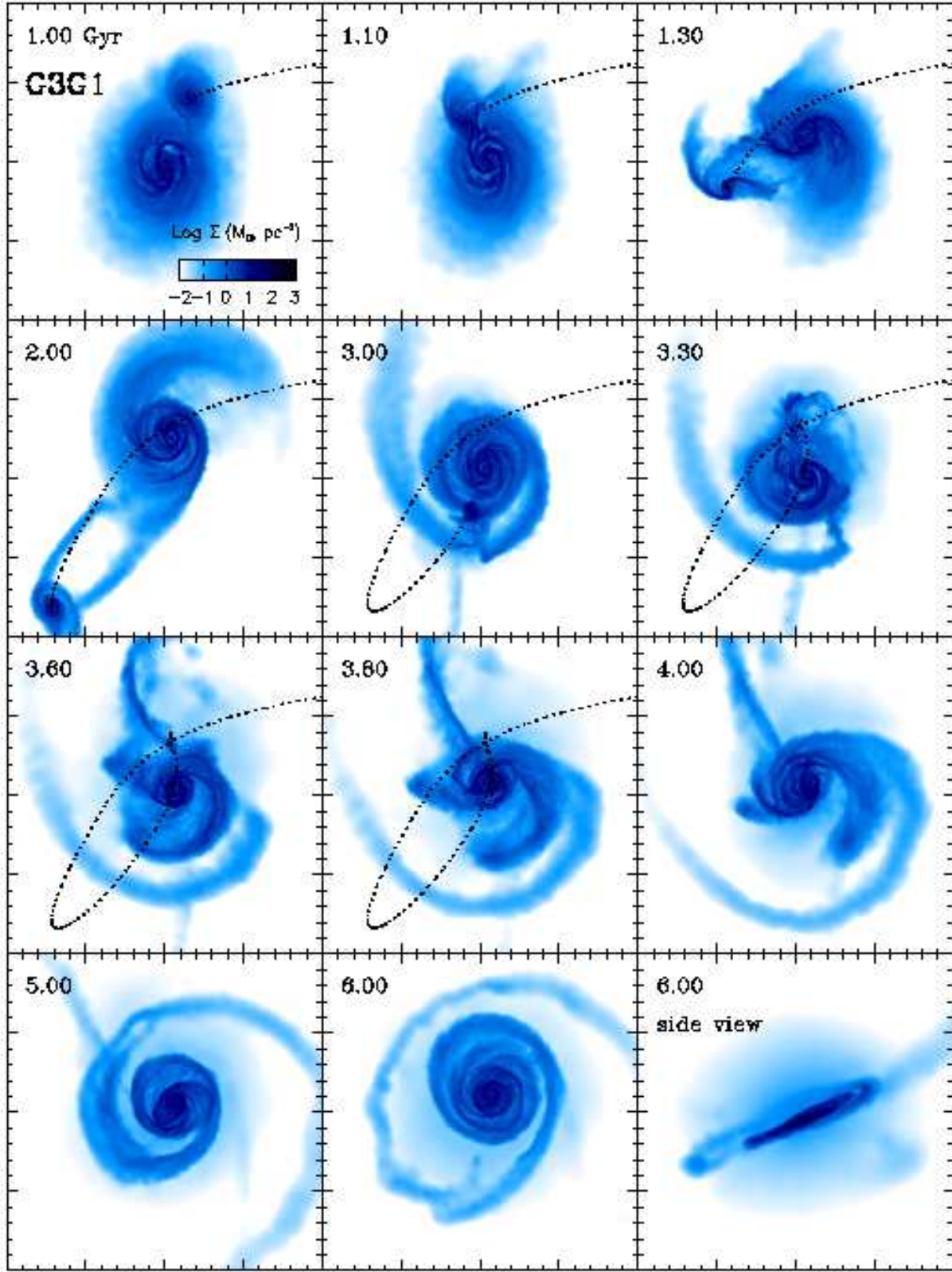


Figure 6. Similar to Figure 6, but for the gaseous component.

Bournaud et al. 2004, 2005). The side views demonstrate that the G3G2 interaction has had a more disruptive effect on the primary’s stellar and gaseous disk than the G3G1 interaction, an unsurprising result given the smaller mass ratio and hence larger tidal disturbance. Furthermore, the gaseous disks are also affected. It is particularly interesting that the G3G1 remnant contains a relatively large, thin gaseous disk, indicating that during an unequal mass interaction the gaseous disk can dissipate its energy and maintain its structure while the stellar disk cannot. The second qualitatively interesting feature is the efficient deposition of the satellite galaxy in the center of the merger remnant. Such a process may be a prominent mechanism to build galactic bulges (see also Aguerrí et al. 2001; Eliche-Moral et al. 2006).

4.3 Star Formation

The star formation history for all of our fiducial galaxy mergers is displayed in Figure 7. There are four plots in this figure, one for each of the four primary galaxy models. The upper-left panel shows the star-formation rate (SFR) for all interactions that involve the most massive galaxy G3. The remaining panels show all the remaining mergers, grouped by the largest participant galaxy. Thus each panels shows the SFR for one major merger and one or more minor mergers, except for the G0G0 panel which only has the G0G0 major merger.

The SFRs shown in Figure 7 are clearly enhanced compared to the quiescent SFRs shown in Figure 2. For example, the maximum SFR during the G3G3 interaction ($\sim 26 \text{ M}_\odot \text{ yr}^{-1}$) is 13 times larger than the summed SFR of two isolated G3 disks ($\sim 1 \text{ M}_\odot \text{ yr}^{-1}$), the maximum SFR during the G3G2 interaction ($\sim 27 \text{ M}_\odot \text{ yr}^{-1}$) is 21 times larger than an isolated G3 ($\sim 1 \text{ M}_\odot \text{ yr}^{-1}$) plus an isolated G2 ($\sim 0.25 \text{ M}_\odot \text{ yr}^{-1}$), and the maximum SFR during the G0G0 interaction ($\sim 3.8 \text{ M}_\odot \text{ yr}^{-1}$) is 3800 times larger than two isolated G0 disks ($\sim 10^{-3} \text{ M}_\odot \text{ yr}^{-1}$), however §4.3.2 demonstrates that these factors depend upon the feedback model.

In §4.4 we will quantify the relationship between the mass ratio of the interacting galaxies and the enhanced star formation in more detail, but we note that this trend fits naturally within a merger-driven scenario for star formation. In particular, during an interaction gas is stripped of its angular momentum by bar-like structures during the early stages of the merger or the abundant collisions and a growing potential well during the messy coalescence. In both cases the resulting central concentration of gas fuels a burst of star formation. Since the tidal forces associated with the merger generate these effects, their magnitude is expected to scale with the size of the perturbation. While this general picture has been studied in great detail for collisions between equal mass galaxies (e.g., Mihos & Hernquist 1994a, 1996; Springel 2000; Cox et al. 2006), we demonstrate here that the star formation clearly depends on the mass ratio of the interacting galaxies.

We caution that the global SFR, as is shown in Figure 7, will be dominated by the largest galaxy when the interacting galaxy mass ratio is large, as in the G3G1 and G3G0 mergers. In this case, the small enhancement in the SFR is only an indication that the primary, G3, is not tidally

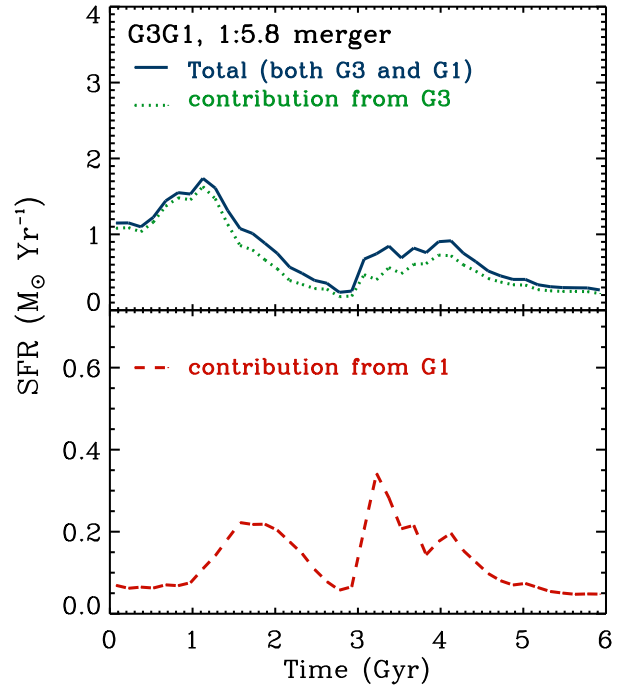


Figure 8. Star-formation rate during G3G1 interaction including the contributions from participant galaxies G3 and G1 separately.

disturbed enough to induce radial inflows of gas and additional star formation. The less massive satellite, however, is expected to experience significant tidal forces and may have a large enhancement of star formation that is hidden within the global rate. Such is the case for G3G1, as shown in Figure 8, where the global SFR is shown as well as the contributions from both the primary and the satellite. While G3, the larger galaxy, constitutes the majority of the overall star formation, its rate is largely unchanged from the initial stages and eventually decays as a result of gas depletion. There is a small enhancement of star formation above the quiescent G3 from $T \approx 3 - 5$ Gyr coincident with the final coalescence. In contrast, the satellite galaxy G1 experiences several bursts of star formation that are > 3 times its quiescent rate, consistent with merger-driven star formation.

The exact relationship between merger mass ratio and enhanced star formation is complicated by the fact that the star formation history also depends upon the nature of the interaction, the structure of the participating galaxies, and the “sub-grid” model for star formation and feedback. The first two dependencies are inherently physical assumptions and will be investigated further in §5. The last dependency, however, is determined by numerical free parameters that are not well constrained. In §4.3.2 this issue will be considered further, with the specific goal of determining which features of the star-formation history provide a measure of the merger-driven star formation that are insensitive to assumptions about the feedback model.

4.3.1 Location of Starburst

One result of merger-driven star formation is a concentration of newly formed stars in the galactic center. Figure 9

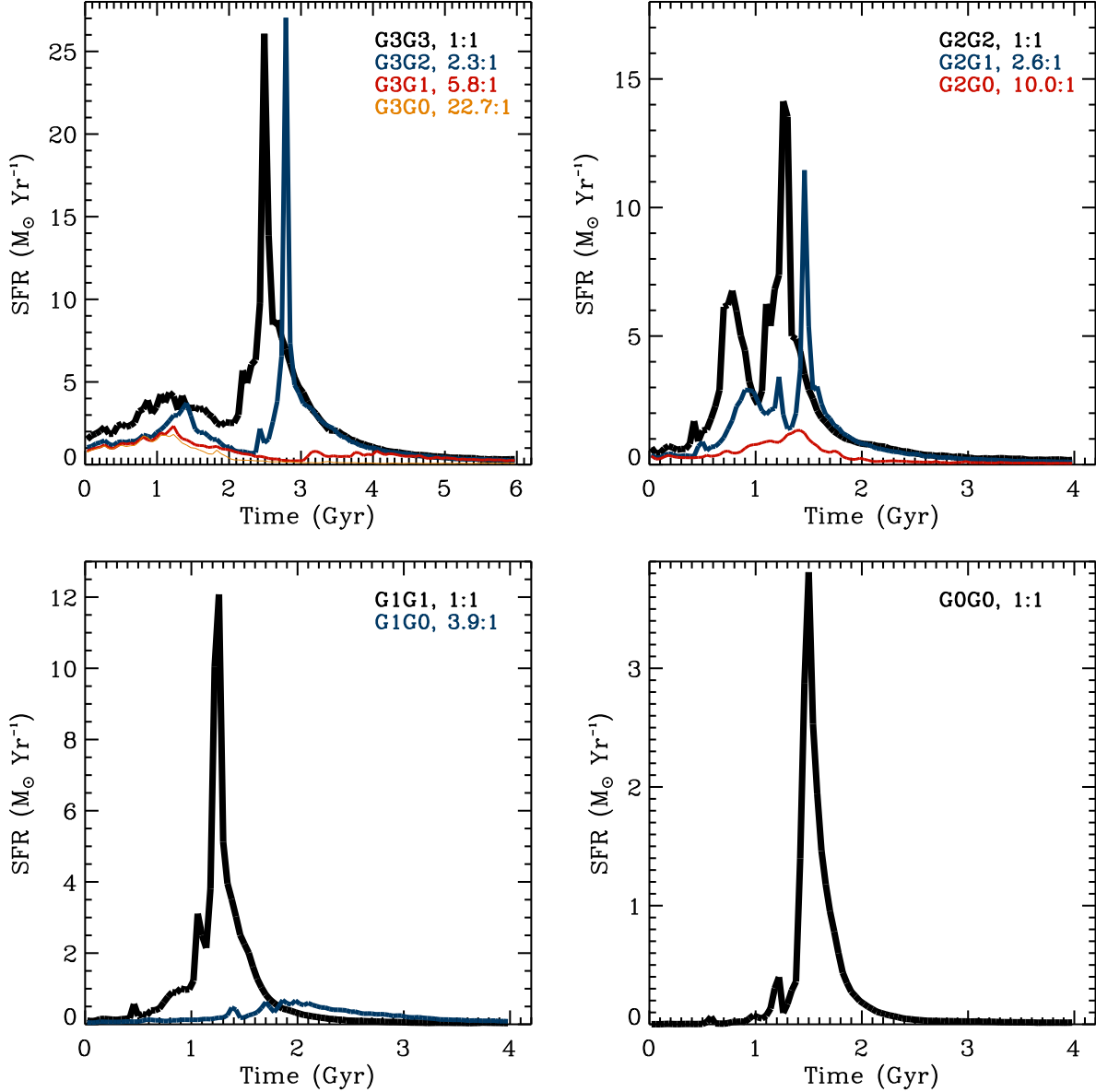


Figure 7. Star formation for our fiducial minor merger series. The total mass ratio is listed next to each run label. The line thickness increases with decreasing mass ratio, e.g., the thickest line in each panel is the 1:1 major merger, while the thinnest line is the large mass ratio minor merger. Note that the vertical axis changes from panel to panel, based upon the maximum star formation rate for the major merger. All runs shown here used the *n0med* feedback model.

demonstrates that this is a generic outcome of our interactions by showing the surface mass density of “new stars,” i.e., stars that form during the interaction, for the remnants of the G3Gx set of interactions. Numerous numerical simulations have previously found similar profiles (though often plotted versus $r^{1/4}$) for remnants of major mergers (e.g., Mihos & Hernquist 1996; Springel 2000; Cox et al. 2006). The central concentrations of new stars are often disjoint from the outer, old-star profiles, in apparent conflict with the $r^{1/4}$ profile that most ellipticals are assumed to have. While this was once considered a problem for the merger hypothesis, recent high-resolution observations now indicate that such features exist in nearly all merger remnants

(Rothberg & Joseph 2004) and many low-luminosity elliptical galaxies (Kormendy et al. 2007).

Because the gaseous inflows that produce these central concentrations of new stars are produced by the gravitational forces arising from the interaction, we expect the amount of new stellar mass in the galactic center to correlate with the merger mass ratio. Indeed, Figure 9 demonstrates that the new star profile within ~ 4 kpc becomes monotonically steeper with decreasing merger mass ratio. The least disruptive mergers, G3G1 and G3G0, have profiles that are essentially exponential beyond ~ 1 kpc, while the smaller mass ratio mergers G3G3 and G3G2 have profiles that are better fit by $r^{1/4}$ -type distributions.

Another way to characterize the distribution of star for-

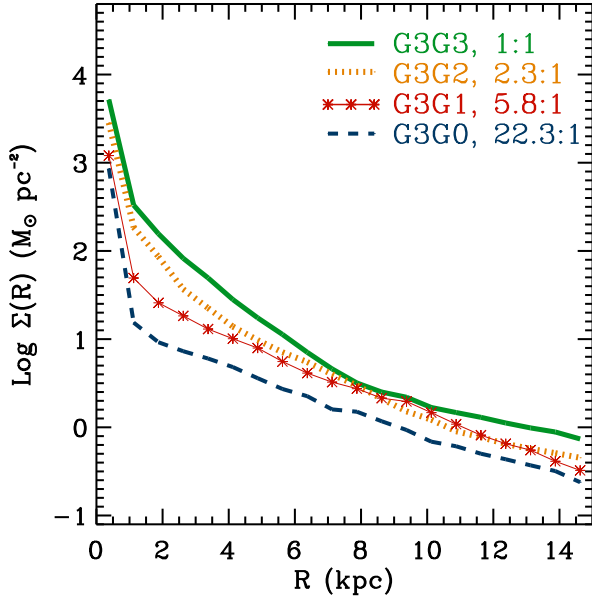


Figure 9. Mass surface density of “new stars,” i.e., stars that are forming during the interaction, for mergers G3G3, G3G2, G3G1, and G3G0.

mation as a result of the interaction is by simply quantifying the fraction of gas that is driven to within the central several hundred pc of the primary. This quantity was an especially relevant measure of the potential starburst event when numerical simulations did not include star formation (e.g., Hernquist 1989; Hernquist & Mihos 1995). In these works it was always found that $> 35\%$ of the gas in the primary was driven to within the central several hundred pc. The only exception was when Hernquist & Mihos (1995) adopted a model in which the interstellar medium was isothermal with a temperature $> 3 \times 10^5$ K. We note that we always find that $< 35\%$ of the gas in the primary is driven to within 500 pc, even during the G3G3 major merger. For the large mass ratio mergers this percentage is closer to 10%, which is similar to the G3 galaxy evolved in isolation. This trend toward smaller inflows of gas is another manifestation of the differences between our modeling and what was performed previously (see more extensive discussion in §6.1).

While it is beyond the scope of the present work, analysis of the remnant profiles uncovers two interesting avenues for future study. First, it is intriguing that the new-star profiles of the remnants of very large mass-ratio mergers are well fitted by a bulge plus exponential disk profile, suggesting that such minor mergers may be an efficient mechanism for growing galactic bulges. Second, at large (~ 10 kpc) radii the profiles of the large mass ratio remnants differ from the G3 evolved in isolation owing to induced star formation and angular momentum transfer during the early stages of the interaction (see also Younger et al. 2007).

4.3.2 Dependence on Star Formation and Feedback Parameters

As mentioned previously (§2 and §4.3), and shown explicitly by Cox et al. (2006) using numerical simulations of major mergers, the star-formation history during an interac-

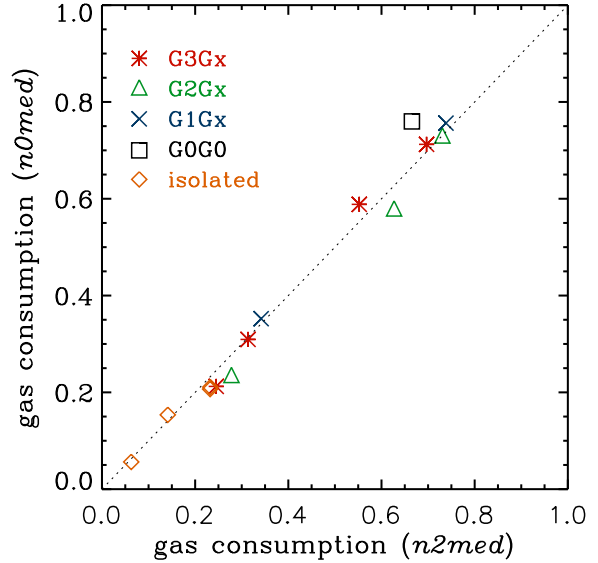


Figure 11. Comparison of the gas consumption during equivalent simulations performed with two different parameterizations for feedback, $n0med$ and $n2med$. The label for the merger simulations are grouped by the primary. The isolated galaxies are identical to the simulations presented in Figures 1 and 2.

tion depends upon the adopted feedback model. This is in contrast to the star-formation history of an isolated spiral, which, as shown in Figure 2 (and in Cox et al. 2006), is independent of the feedback model. As a result, it is unclear what measure of the star-formation history will provide a robust characterization of the merger-driven star formation. To investigate this further, we resimulated our fiducial set of mergers using the $n2med$ feedback model in addition to the $n0med$ that was presented in §4.3. As shown in Cox et al. (2006), the “medium” feedback models are slightly favored because they can maintain a stable gas disk in an isolated gas-rich Sbc galaxy model and also produce merger-driven starbursts. The $n0med$ model treats star-forming gas with an isothermal ($\sim 10^5$ K) equation of state while the $n2med$ has a stiff equation of state that restricts the quantity of gas at very high densities.

Figure 10 shows the SFR and gas consumption during the G3G2, G3G1, and G3G0 unequal mass mergers for both the $n0med$ and $n2med$ feedback models. For all interactions the peak of star formation begins sooner, has a much larger maximum, and a shorter duration in the $n0med$ feedback model as opposed to $n2med$. However, regardless of the differences in the star-formation history, the gas consumption is very similar, as shown for the full series of merger simulations in Figure 11. This result motivates us to focus our analysis upon quantities that use the gas consumption rather than details of the time-dependent star-formation history, since the gas consumption is invariant to assumptions about the feedback model. We also note that the non-equivalence in gas consumption between the two feedback models that is present in Figure 11 can be used to estimate our errors owing to adopting a single feedback model. From the standard deviation in discrepancies we estimate an error of ~ 0.04 in the gas consumption owing to the choice of feedback model.

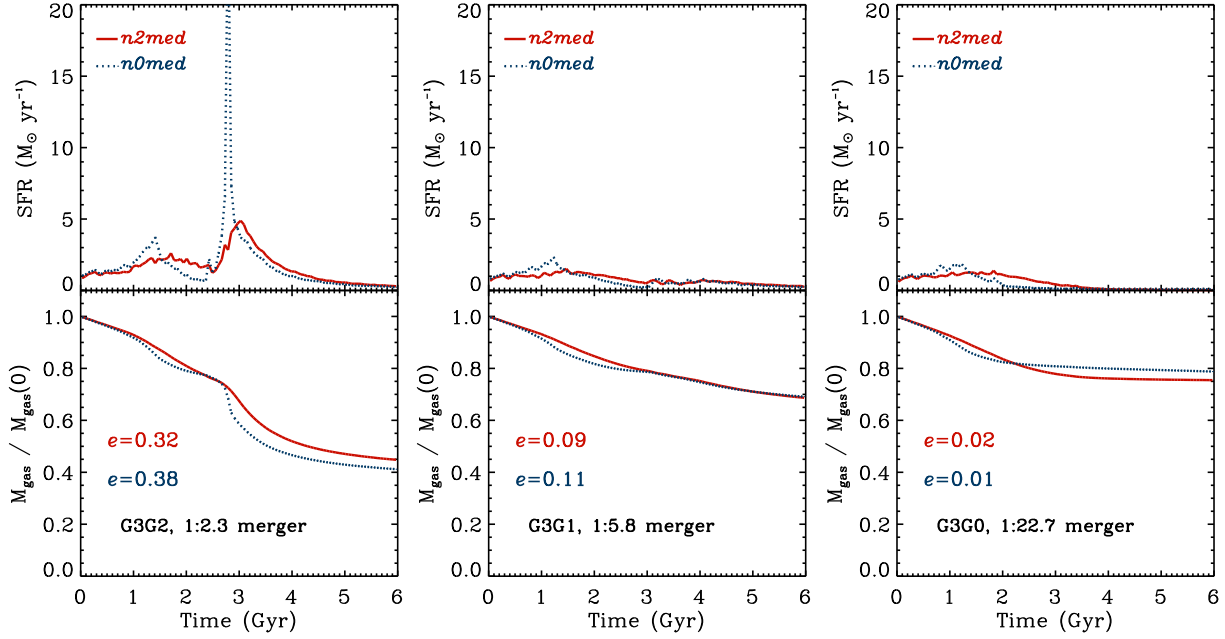


Figure 10. Comparison between two parameterization of star formation and feedback in identical unequal mass mergers. The top panels show the star-formation rate, and the bottom panels show the gas consumption. In general, details of the star-formation history depend on the feedback model while the gas consumption remains relatively invariant. The burst efficiency (see §4.4.1) of each run (*n2med* on top, and *n0med* on the bottom) is provided in the lower panel.

However, we also caution that 3 out of the 4 major mergers have slightly (< 0.1) higher gas consumption when adopting the *n0med* feedback model, and the 2 minor mergers with the largest mass ratios have higher gas consumption when adopting the *n2med* feedback model. Therefore, it is possible that subtle, yet systematic, trends exist between alternate feedback models.

As a final comment we note that Figure 10 demonstrates that the feedback model can drastically affect the time-dependent star-formation rate, and therefore the luminosity of the system, even though the total gas consumption is similar. The varying luminosity evolution admits the possibility to better constrain the feedback model through a comparison to the observed distribution of star-formation rates (see, e.g., Noeske & al. 2007).

4.3.3 The Star-Formation Timescale

The previous section demonstrates that each feedback model yields a unique star formation history, and noted that one difference between the histories is the star-formation timescale. Because differences in the star-formation timescale directly affect the predicted color, line-strength, and nuclear activity of the interacting pair, future work may have the ability to discriminate between feedback models based upon comparisons with observations (e.g., Barton et al. 2000; Nikolic et al. 2004; Woods et al. 2006; Geller et al. 2006; Woods & Geller 2007; Ellison et al. 2007; Barton et al. 2007).

As a preliminary step toward this goal, we quantify the starburst timescale for the mergers simulated here from three different fits to the starburst events. The first fit is motivated by the intrinsic shape of the starburst events as

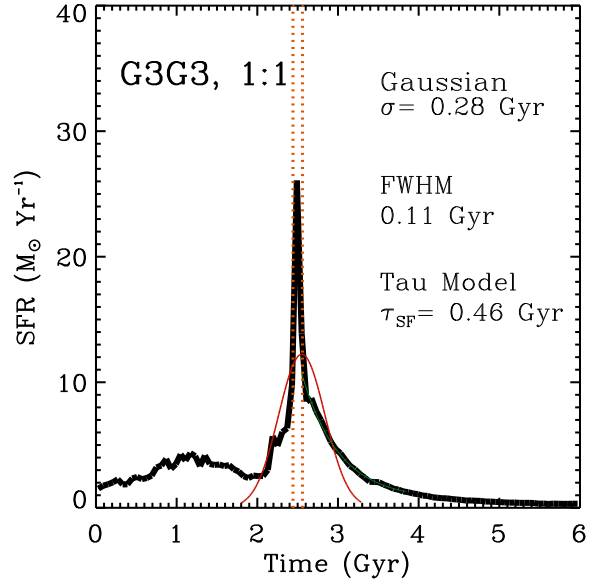


Figure 12. Star-formation rate during the G3G3 major merger with the *n0med* feedback parameters (thick solid line). Overplotted are three characterizations of the merger timescale, one, a single Gaussian fit to the merger-induced peak of star formation (thin solid line), two, a decaying exponential fit to the star-formation rate after the peak of star formation and, three, the full width at half maximum (vertical dashed lines).

exemplified in Figures 7 and 10, namely they appear Gaussian in shape and their timescale can be characterized by the width σ . The second fit is motivated by many models of galaxy evolution that describe star formation as a decay-

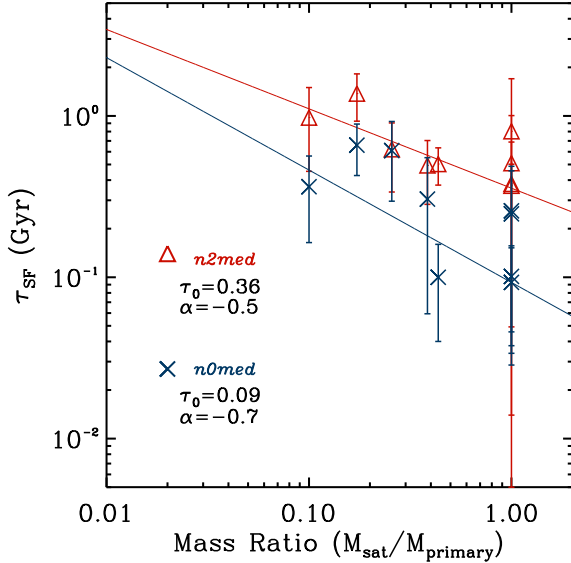


Figure 13. The star formation timescale (τ_{SF}) as a function of merger mass ratio for our fiducial series of mergers when simulated with both the *n0med* and *n2med* feedback models. The timescale is the average of the three fits (Gaussian, exponential, and FWHM) scaled to the exponential decay timescale τ and the errors are estimated by the dispersion between the three fit parameters. The solid lines are fits to the simulated data using Equation 3.

ing exponential with a timescale τ , and are therefore often described as “tau”-models (see, e.g., Somerville & Primack 1999; Harker et al. 2006; Noeske & al. 2007). The last method to describe the star formation timescale calculates the full width at half maximum (FWHM) and therefore avoids any biases associated with adopting a specified distribution for the starburst. Another possibility, which we reserve for future work, is to compile the full luminosity distribution for the entire merger as has been done previously by Jonsson (2004) and Hopkins et al. (2006).

As an example of a starburst event, and its corresponding fits, we show the merger G3G3 in Figure 12. Printed directly on the figure are estimates for the starburst timescale that result from each fit. The three separate timescale measures can be placed on an equal footing by noting that the FWHM of a Gaussian distribution is 2.35σ , and fitting an decaying exponential to one side of a Gaussian yields $\tau \approx 1.1\sigma$. For this particular case, the starburst has a distinct peak and extended tails compared to the Gaussian fit (i.e., a positive Kurtosis). Therefore, the timescale derived from the FWHM is much smaller than that derived from the Gaussian fit. The starburst is very well-fitted by the tau-model (so much so that the fit is difficult to see in Figure 12) which yields a slightly longer estimate of the star formation timescale.

In general, we note that nearly all models that employ the *n0med* feedback have peaky star formation, and thus small FWHMs compared to the Gaussian or exponential estimates. However, because the star formation events are typically irregular, we consider the best estimate of the star formation timescale to be an average between τ , 1.1σ , and

0.47FWHM , i.e., the estimates from the different fits are all scaled to be in terms of the exponential decay timescale τ . This also provides a simple estimate of the error in our fitting procedure from the dispersion among the three determinations of the timescale.

In Figure 13 we plot the estimates for the star formation timescale and the associated errors for the fiducial set of runs as a function of merger mass ratio for both feedback models. To characterize the mass-ratio dependence, we have fit a simple power-law to the mergers of each feedback model, viz.,

$$\tau_{\text{SF}} = \tau_0 \left(\frac{M_{\text{sat}}}{M_{\text{primary}}} \right)^\alpha. \quad (3)$$

Confirming our visual inspection of the SFRs shown in Figure 10, the *n2med* model has a much longer star-formation timescale than the *n0med* model. In addition, both models display a trend for the star-formation timescale to increase with increasing mass ratio, however the uncertainties are large enough that this trend is not definitive. In particular, the goodness of fit is only slightly reduced if the fit is fixed to have no mass-ratio dependence at all ($\alpha = 0$).

4.4 Parameterizing Star Formation Enhancements During Galaxy Interactions

The star-formation histories shown in Figure 7 demonstrate clear signs of enhanced star formation during the merger. Furthermore, §4.3.2 argues that this enhanced star formation is more robustly characterized by the amount of gas consumed, rather than time-dependent quantities such as the maximum star formation rate, owing to uncertainties in the adopted feedback model. However, we must also consider that the two galaxies which participate in the interaction would have converted some of their available gas into stars even in isolation, and therefore the gas consumption itself does not provide a complete characterization of the merger-driven star formation.

A more explicit comparison between the merger-driven star formation and that of the isolated disks is presented in Figure 14, which shows several measures of star formation for the G3G3, G3G2, G3G1, and G3G0 mergers, in each column, from left to right, respectively. The top row presents the star-formation rate (SFR) for the merger as well as the summed SFR of the primary and satellite galaxies when evolved in isolation. For clarity, the difference between the two SFRs is shaded. The second row shows the ratio of the merger SFR to the combined SFR of the isolated galaxies, clearly delineating when the rate is enhanced owing to the merger. The third row plots both SFRs divided by the stellar mass, which is also the inverse of the stellar-mass doubling time, and is sometimes termed the “specific SFR.” The fourth row plots the SFRs divided by the gas mass, which is the inverse of the gas consumption timescale. Finally, the bottom row presents the gas consumption of both the merger and the combined isolated galaxies with the difference shaded.

There are several features present in Figure 14 that deserve more discussion. First, reinforcing the notion first presented in Figure 7, there is a clear correlation between interacting galaxy mass ratio and merger-driven star formation. Significant episodes of star formation only occur for mergers

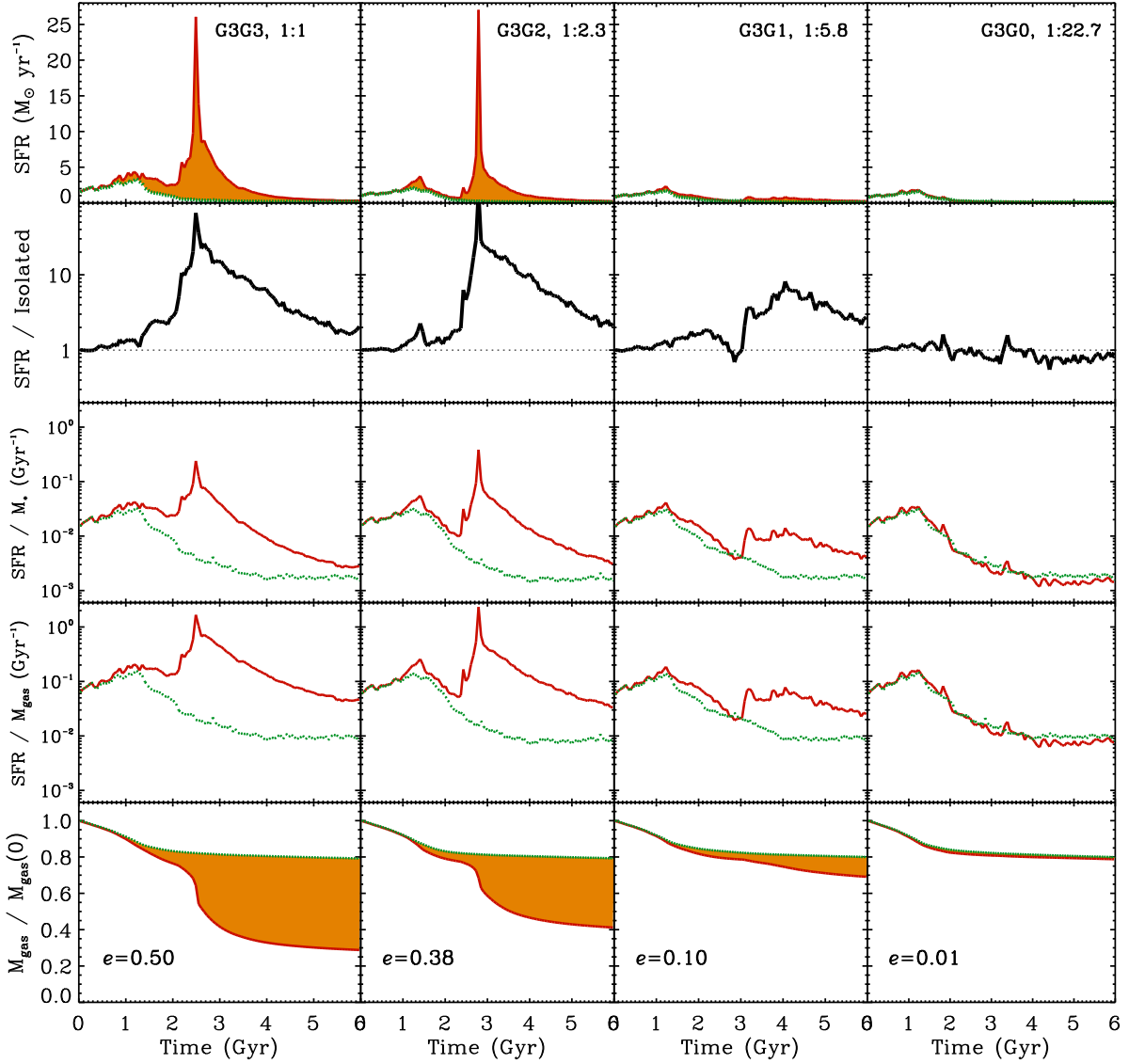


Figure 14. The rows from top to bottom show the star-formation rate (SFR), SFR normalized by the combined SFR of both isolated galaxies, the SFR divided by the total stellar mass, the SFR divided by the total gas mass, and the gas consumption for mergers G3G3, G3G2, G3G1, and G3G0, from left to right. Panels show quantities during the interaction with a solid (red) line and for the combined isolated galaxies with a dotted (green) line. The difference between the two lines is shaded to emphasize the merger-driven star formation. All simulations shown employ the *n0med* feedback model. The burst efficiency (see §4.4.1) is printed in the bottom row for each interaction.

between galaxies of nearly equal mass. For mergers between galaxies with a large mass ratio, such as G3G0, the cumulative star-formation history is nearly indistinguishable from the primary G3 evolved in isolation.

By comparing the star-formation history of G3G3 to that of G3G2, we uncover another interesting feature of Figure 14. Namely, these two interactions have similar peak levels of star formation, even though the total amount of gas consumed is much less for the higher mass ratio G3G2 interaction. This feature of the star-formation history emphasizes that caution needs to be exercised when attempting to quantify the merger-driven star formation.

As a final comment, we note that all models except G3G0 show elevated star formation at the end of the inter-

action ($T \approx 6$ Gyr) compared to the primary G3 evolved in isolation, as indicated by the normalized SFR shown in the second row of Figure 14. Therefore, most measures of the merger-driven star formation are subject to uncertainties that depend upon the duration over which the simulations follow the merger (if the simulation was run for long enough, all galaxies would consume essentially all of their initial allotment of gas). In practice, these errors are quite small, which we estimate to be ~ 0.03 from the differential gas consumption (bottom row of Figure 14) if the simulation is followed for 1 Gyr prior to, or later than, the current 6 Gyr we adopt as a standard.

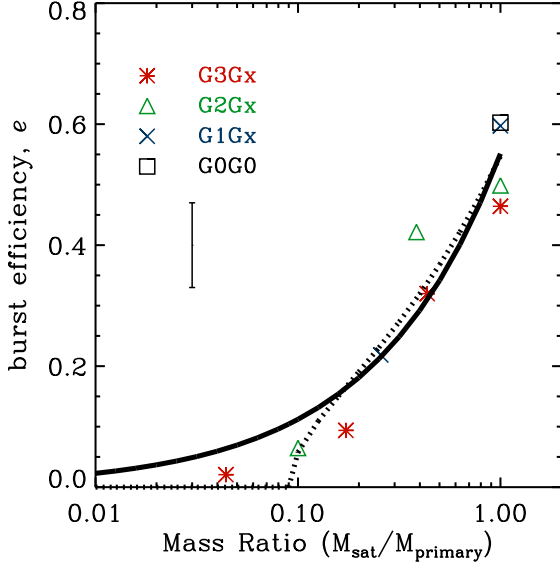


Figure 15. Burst efficiency e (defined in Eq. 4) for all fiducial merger simulations. Interactions in which G3 was the largest progenitor, i.e., G3Gx, are shown with a (red) asterisk, while G2Gx mergers are (green) open triangles, G1Gx are (blue) X's, and G0G0 is an open (black) square. The solid line is the best-fit relation using Eq. 5, and the dotted line is the best-fit relation using Eq. 6. The vertical line below the key shows our estimated error in burst efficiency of ± 0.07 owing to uncertainties in the feedback model and the duration in which the simulation is followed.

4.4.1 Burst Efficiency

In order to quantify the merger-driven star formation, we wish to define a simple, useful, and robust parameterization of the star formation owing solely to the interaction. To this end, we are motivated by the discussion of §4.3.2 to introduce the “burst efficiency” e , as

$$e = \left(\text{fraction of gas consumed during interaction} - \text{fraction of gas consumed by constituent galaxies evolved in isolation, during the same time period} \right) \quad (4)$$

The burst efficiency is the fractional amount of stars that are formed (or equivalently, the gas that is consumed) during the merger that would not have formed in isolation. Figure 15 shows the burst efficiency for our fiducial merger series and reaffirms what was implicit in Figures 7 and 14; namely, merger-driven star formation is only significant during mergers where the participating galaxies are comparable in mass.

The burst efficiency appears to be a smoothly decreasing function of the merger mass ratio and its parameterization may be useful for future studies of galaxy formation. In fact, such a parameterization has already been introduced by Somerville, Primack & Faber (2001, see their Fig. 1) based upon a much smaller set of data (the simulations of Mihos & Hernquist 1994a, 1996), and used in their semi-analytic models. Following Somerville et al. (2001), we adopt the following form for the burst efficiency:

$$e = e_{1:1} \left(\frac{M_{\text{sat}}}{M_{\text{primary}}} \right)^{\gamma} \quad (5)$$

where $e_{1:1}$ is the burst efficiency for equal mass mergers, M_{sat} and M_{primary} are the mass of the satellite and primary, respectively, and γ fixes the mass ratio dependence. Performing a least-squares fit to our entire set of fiducial mergers we find $e_{1:1}=0.55$ and $\gamma=0.69$. This fit is shown as a solid line in Figure 15.

Owing to the relatively small star-formation enhancement in large mass ratio mergers ($M_{\text{sat}}/M_{\text{primary}} < 0.2$), and the systematic overestimate in the regime provided by the best-fit Eq. 5, we also consider an alternate form for the burst efficiency that is fixed to zero when the mass ratio $M_{\text{sat}}/M_{\text{primary}}$ is below e_0 and is

$$e = \left(\frac{M_{\text{sat}}}{M_{\text{primary}}} - e_0 \right)^{\gamma}, \quad (6)$$

when the mass ratio $M_{\text{sat}}/M_{\text{primary}}$ is greater than e_0 . Performing a least squares fit to our fiducial mergers yields $e_{1:1}=0.56$, $\gamma=0.50$, and $e_0=0.09$, although the reduced χ^2 is nearly unchanged if e_0 is manually set to anything less than 0.11 (including 0, in which case the fit is identical to Eq. 5). In other words, our fiducial set of mergers are consistent with there being no enhancement of star formation below a mass ratio of 9:1, although the data doesn’t necessarily require this. The best fit to Eq. 6 is shown in Figure 15 as a dotted line.

A number of other fitting formula are also possible for the burst efficiency, such as single and broken power-laws, and various polynomials, however with the small number of data points and the associated uncertainties in calculating the burst efficiency, no one formula was statistically better than any other formula. Hence, we adopt Eq. 5 to describe the burst efficiency.

For comparison, the Somerville et al. (2001) fit to the Mihos & Hernquist data using Eq. 5 yielded $e_{1:1} = 0.75$ and $\gamma = 0.18$, when the progenitor disks did not include a stellar bulge, and $e_{1:1} = 0.75$ and $\gamma = 1.16$ when they did. The consistency of $e_{1:1}$ indicates that the presence of a bulge does not affect the burst efficiency of major mergers. We also note that a value of 0.75 for $e_{1:1}$ is about 50% larger than our preferred value, indicating that the models employed here are less efficient at turning gas into stars than those of Mihos & Hernquist. In fact, this difference is similar to that found previously by Cox et al. (2006) who showed that the feedback model and the newer version of SPH employed produce these changes. Our value of γ is between the Somerville et al. (2001) value, a trend that is likely driven by the fact that our primary galaxy G3 has a bulge-to-disk ratio that is lower than in their model. We will attempt to explore these dependencies in more detail in the following section.

5 ADDITIONAL MERGER SIMULATIONS

The previous section detailed the outcome of 10 mergers, including 6 unequal mass mergers, between our four galaxy models. In this section we perform a number of additional merger simulations in order to explore several interesting, and particularly relevant regions of parameter space; the merging orbit and the structure of the progenitor disk, specifically the extent of the gaseous disk, the bulge-to-disk ratio, and the gas fraction of the progenitor disk.

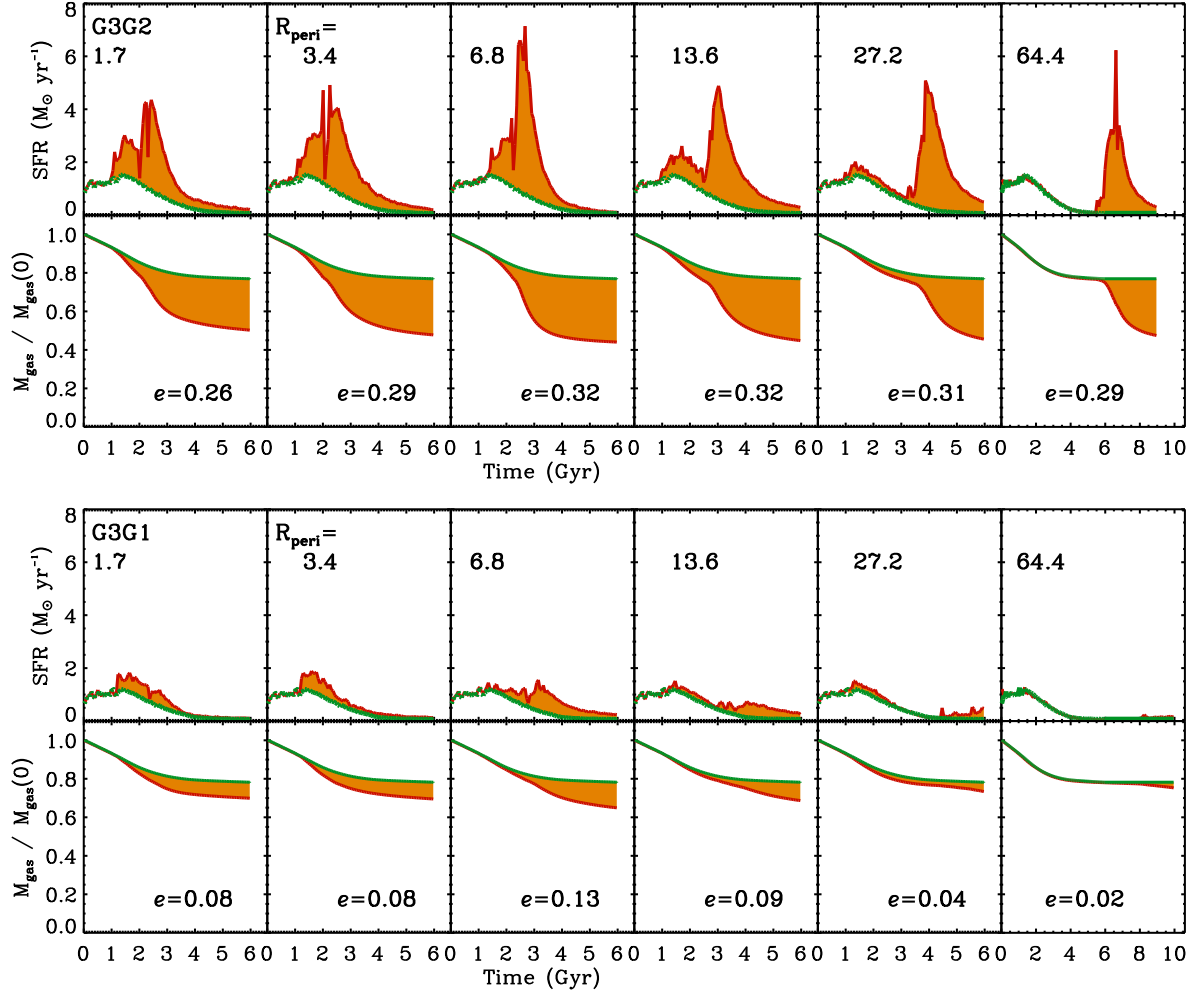


Figure 16. Star-formation history and gas consumption for the G3G2 (top) and G3G1 (bottom) unequal mass interactions when merged on orbits that have varying amounts of angular momentum, as set by the pericentric distance R_{peri} , which is listed in the top of each column in units of kpc. All merger orbits are inclined by 30° and nearly parabolic (eccentricity 0.95). The fiducial encounters all assumed $R_{\text{peri}} = 13.6$ kpc when the primary was G3. The burst efficiency is listed in the bottom of each column. All mergers use the *n2med* feedback model.

5.1 Variations in Orbit

As outlined previously (§1 and §4.3), the enhancement of star formation during galaxy interactions originates from tidal forces that attend the merger. In particular, the close passage between the interacting galaxies produces bar-like structures in the *stellar* disk that torque gas into the galaxy center. Figure 8 shows that this occurs in both the primary and the satellite. The nearly prograde mergers that we have tracked up to this point produce a relatively strong bar owing to resonances between the orbits of stars in the primary disk and the passage of the satellite galaxy. However, alternative orbits and orientations of the interaction will affect the strength of the tidal force as well as the resonances excited within the disk, and therefore the resulting starburst.

To determine how the star-formation history depends upon the orbital angular momentum and disk orientation of the merging galaxies we have run two series of interactions using the G3G2 and G3G1 mergers. In the first series, we systematically change the orbital angular momentum which, in practice, is modulated by the pericentric distance R_{peri} .

All other parameters are identical to the fiducial mergers. The star-formation histories and gas consumption fractions resulting from this set of mergers are shown in Figure 16. For both the G3G2 and G3G1 interactions the maximum gas consumption occurs when $R_{\text{peri}} = 6.8$ kpc, or roughly $(6.8/2.85 \approx) 2.4$ times the stellar scale radius of G3. The increasing gas consumption for more direct interactions supports the connection between tidal forces and merger-driven star formation. We also note that the two interactions with R_{peri} less than 6.8 kpc consume slightly less gas than orbits with larger R_{peri} . This trend is likely a result of the disruptive nature of nearly head-on collisions as well the difficulty of capturing shock-induced star formation within SPH (although recent star formation models have been formulated to address this shortcoming; Barnes (see, e.g., 2004)).

The second series of runs systematically alters the satellite orientation. While the fiducial set of mergers assumes that the orbital plane was inclined by 30° with respect to the disk of the primary galaxy, this series varied the inclination. A range of mergers are performed in which the incli-

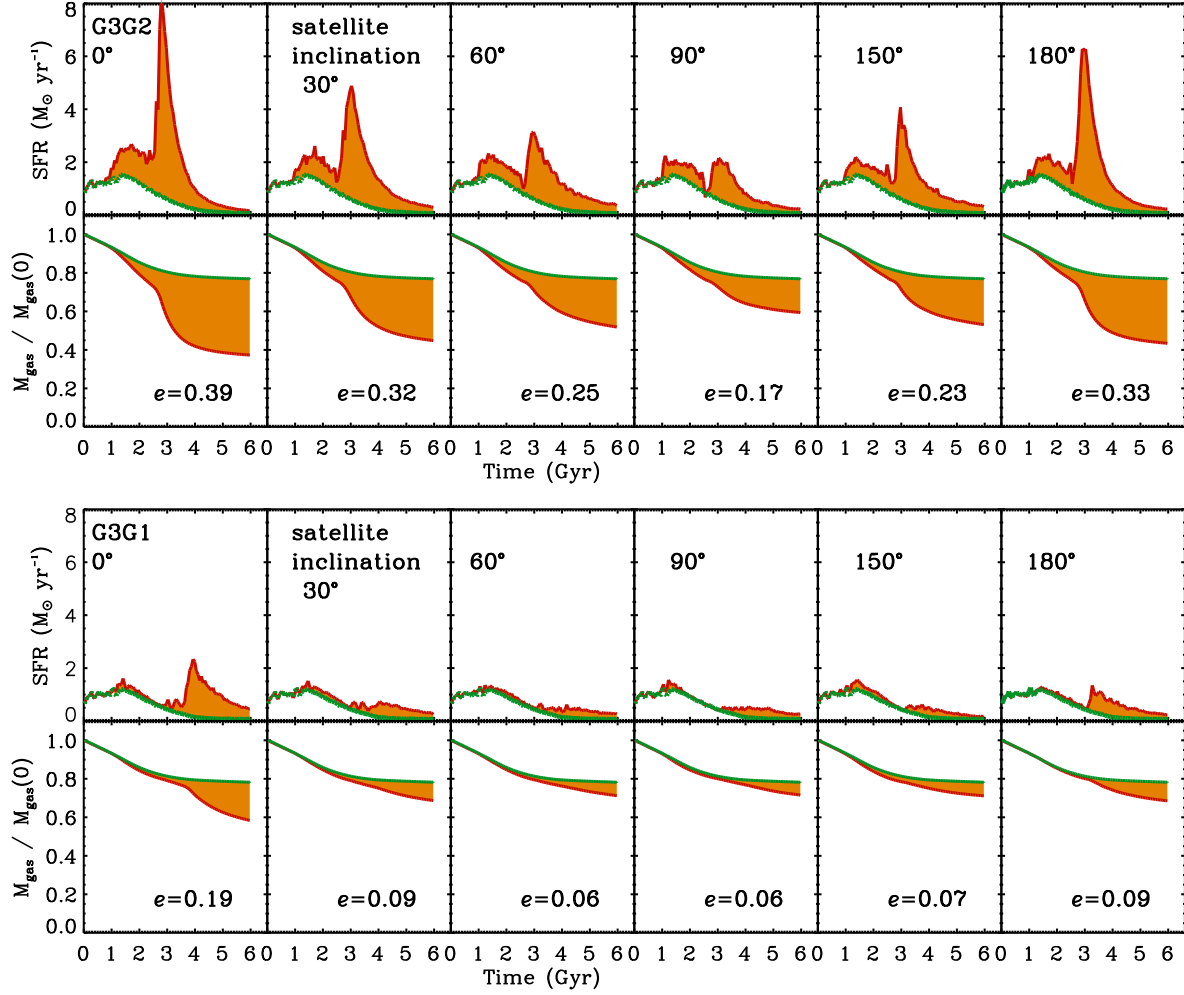


Figure 17. Star-formation history and gas consumption for the G3G2 (top) and G3G1 (bottom) unequal mass interactions when merged on orbits that have varying satellite orientations, from 0° (a perfectly prograde encounter) to 180° (a perfectly retrograde encounter). The other parameters of the merging orbits are similar to the fiducial case, i.e., they are nearly parabolic (eccentricity 0.95) and have moderate angular momentum ($R_{\text{peri}} = 13.6$ kpc). Note that the fiducial set of mergers were inclined by 30° . The burst efficiency is listed in the bottom of each column. All mergers use the *n2med* feedback model.

nation is prograde (0°), polar (90°), and retrograde (180°), as well as several in between. Figure 17 shows the resulting star formation and gas consumption for these runs. As expected, mergers in which the orbit of the secondary is aligned with the primary disk, i.e., prograde orientations, produce the strongest tidal responses in the disk and therefore the largest bursts of star formation.

It is likely that similar results would follow from other orbital explorations, such as the initial separation between the two galaxies, as well as the energy of the initial orbit. Interestingly, the largest starburst event in the series of major merger interaction studied by Cox (2004) was a zero net angular momentum orbit. In short, we expect any factor that efficiently strips gas of its angular momentum, including collisions, or increasing the tidal coupling between the satellite orbital motion and stars in the disk of the primary will lead to the most substantial bursts of star formation.

5.2 Variations in the Extent of Gaseous Disk

Motivated by observations (see, e.g., Broeils & van Woerden 1994), the galaxy models that form the basis for this work assume that the distribution of gas in the disk is more extended than the stars. Specifically, the gas has an exponential scale radius $\alpha = 3$ times that of the stellar disk. As a result, there is a significant quantity of gas at large radii. This extended gas does not significantly contribute to the nuclear starburst. Instead, the merger remnant contains a large quantity of gas in both a shock-heated hot phase (Struck 1997; Cox et al. 2004, 2006) as well as in a cold star-forming disk.

In order to discern how the assumed distribution of gas influences the burst efficiency, we have run a number of tests that alter the distribution of cold gas in the primary G3 galaxy. Figure 18 shows an example of our typical result, namely, the extended gas distribution leads to an increased estimate of the burst efficiency. For the case shown in Figure 18, the fiducial G3 galaxy model has been altered to have

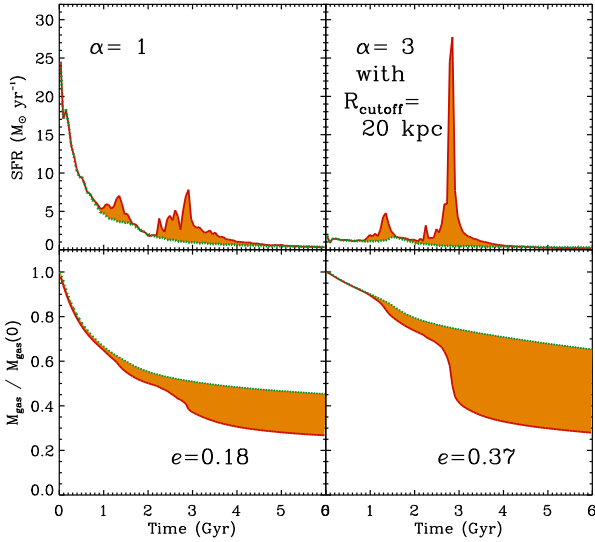


Figure 18. Star formation and gas consumption for two G3G2 mergers. The case on the left is similar to the fiducial interaction except the primary G3 galaxy model now has $\alpha = 1$, where α is the multiplicative factor that sets the scale radius of the gaseous disk with respect to the stellar disk (see §3). The case on the right is also similar to the fiducial interaction except the primary G3 galaxy model has $\alpha = 3$ and all gas beyond 20 kpc has been removed from the initial disk. The burst efficiency is indicated in the bottom panel for each case. Both mergers are run using the *n0med* feedback model.

$\alpha = 1$, while keeping the remaining parameters, including the total gas mass, unchanged. In short, the vigorous star formation in the isolated primary consumes a larger fraction of the available gas and results in a lower burst efficiency.

In additional experiments we merged models with the fiducial G3 distribution of gas ($\alpha = 3$), however all gas beyond a cutoff radius (R_{cutoff}) is removed. In essence, these galaxy models have much less gas, yet the inner, star-forming gas distribution is unchanged. As shown in Figure 18, the resulting star-formation histories are unchanged. Even though the fractional gas consumption increases markedly (compared to the second column in Figure 14), owing to a corresponding increase in the gas consumption of the isolated system, the resulting burst efficiencies are nearly identical. These experiments indicate that the burst efficiency is predominantly a function of the density distribution of gas in the progenitor systems rather than purely the spatial distribution of gas.

5.3 Variations in Bulge-to-Disk Ratio

One of the most significant results from the work of Mihos & Hernquist (1994a, 1996) was the discovery that the internal structure of the primary galaxy can strongly influence the efficiency of the starburst. Specifically, these works showed that a massive stellar bulge stabilizes the disk against tidal perturbations and suppress strong inflows of gas that lead to starbursts. In the case of minor mergers, the presence of a bulge may eliminate the merger-driven starburst completely, while during a major merger the bulge may simply delay the starburst until the final coalescence of the two galaxies.

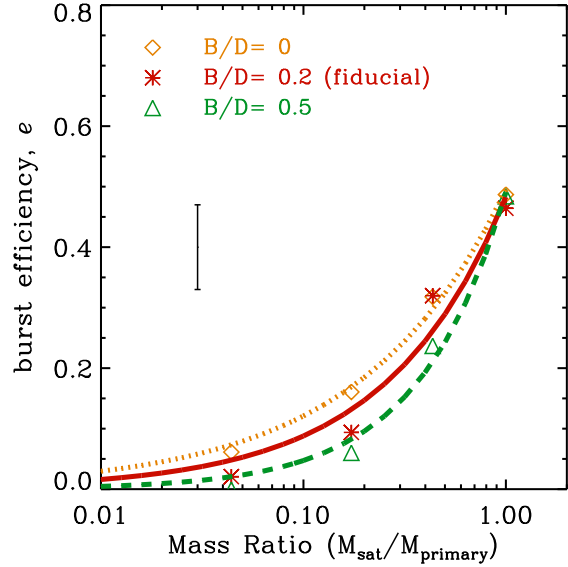


Figure 19. Similar to Figure 15 except here the burst efficiency is shown for three series of runs with different values of the bulge-to-disk ratio (B/D) in the primary G3 galaxy.

The absence of any discernible burst of star-formation for the G3G1 and G3G0 minor mergers presented in §4 support the notion that the presence of a stellar bulge can suppress merger-driven star formation when the mass ratio is large. Furthermore, this burst suppression persists even though the bulge adopted for the fiducial G3 model is only 20% the mass of the stellar disk, i.e., the bulge-to-disk ratio (B/D) is 0.2, or about 50% smaller than in the models of Mihos & Hernquist where $B/D = 0.33$. In order to provide a more direct comparison to their work and further assess the effects of bulge mass on the merger-driven starburst, we have run a number of additional interactions where the bulge mass of the fiducial G3 model is altered such that there is no bulge at all ($B/D = 0.0$), or where the bulge mass is increased by a factor of 2.5 ($B/D = 0.5$). All other parameters, including the fiducial merging orbits and the satellite galaxies (G2, G1, and G0), are left unchanged.

Figure 19 shows the burst efficiency as a function of merger mass ratio for our series of mergers in which the bulge mass of the G3 primary is varied. As expected, there is a systematic correlation for large mass ratio mergers to have smaller burst efficiencies when the bulge mass increases. For example, the bulgeless G3G1 (5.8:1) merger has a burst efficiency of 0.16, which is three times larger than the burst efficiency for the model with the most massive bulge ($B/D = 0.5$). We also note that the burst efficiency is insensitive to the bulge mass when the merger mass ratio is near unity, in agreement with Mihos & Hernquist (1996).

Using Eq. 5, the best fit to each series of B/D mergers is determined and overplotted in Figure 19. All fits have the identical value of $e_{1:1}$, 0.49, a result of the constant burst efficiency during major mergers. The value of γ , which sets the mass ratio dependence, is 0.61, 0.74, and 1.02 for the series with $B/D = 0.0$, 0.2 (the fiducial), and 0.5, respectively. It should be pointed out that the best fit for the fiducial se-

ries is slightly different than that reported in §4.4.1 because here only the G3Gx series is analyzed.

Even though the qualitative relationship between bulge mass and burst efficiency is in agreement with Mihos & Hernquist (1994a), their bulgeless minor merger produced a significant burst of star formation. The result is a burst efficiency (~ 0.7) that is much larger than *any* of our interactions, major or minor. This discrepancy was also noted in §4.4.1, and is likely a result of three differences between their modeling and ours.

First, the feedback model and the newer entropy-conserving version of SPH employed here both result in less intense episodes of merger-driven star formation (Cox et al. 2006). Second, the models employed by Mihos & Hernquist adopt a circular orbit for the satellite, which increases the tidal coupling to stars in the disk and produces a larger response. Lastly, the large burst efficiency found by Mihos & Hernquist is inflated by the very inefficient star formation assumed to occur in their quiescent disk. Such levels of star formation appear to be insufficient to match more recent observations (Kennicutt 1998).

While these three arguments outline why our burst efficiencies are more modest — and we believe, more accurate — than prior calculations, the previous sections of this paper suggest that a number of the parameters for our fiducial encounters are sub-optimal at producing the largest merger-driven star formation event (and hence burst efficiency). We therefore performed a small number of additional simulations using a bulgeless version of our fiducial G3G1 merger, only we placed the satellite G1 on a co-planar (0°), close passage ($R_{\text{peri}} = 6.8$ kpc) orbit in order to maximize the merger-induced starburst (this orbit was motivated by the results of §5.1).

The star-formation history during the interaction with the maximum burst efficiency, as determined from our small G3G1 parameter search, is shown in Figure 20. We have also shown corresponding interactions when the modified bulgeless G3 model has bulge-to-disk ratios of 0.2, similar to the fiducial G3 model, and 0.5. Even with the large degree of parameter manipulation the maximum burst efficiency for the bulgeless run is only 0.19. While this is $\sim 20\%$ larger than the the bulgeless G3G1 in the fiducial encounter, and about ~ 4 times the fiducial G3G1 merger, it is still far below the ~ 0.70 found by Mihos & Hernquist (1994a).

5.4 Variations in Gas Fraction

In our final set of additional merger simulations, we vary the gas fraction of our fiducial G3 galaxy model. To this end, the total mass in the disk is kept fixed, yet the distribution of mass, i.e. the amount in the gaseous versus the stellar disk, is varied for each model. All other parameters, including the interaction orbit and the satellite galaxies (G2, G1, and G0) remain unchanged from their fiducial values. Figure 21 presents the star formation history, the gas consumption, and the burst efficiency for the fiducial G3G2 interaction plus two additional mergers when the G3 primary has a larger gas fraction, f , defined as the mass of the gas disk divided by the total (gas plus stars) disk mass.

Figure 21 exemplifies the generic outcome of all interactions that test the gas fraction of the primary, namely,

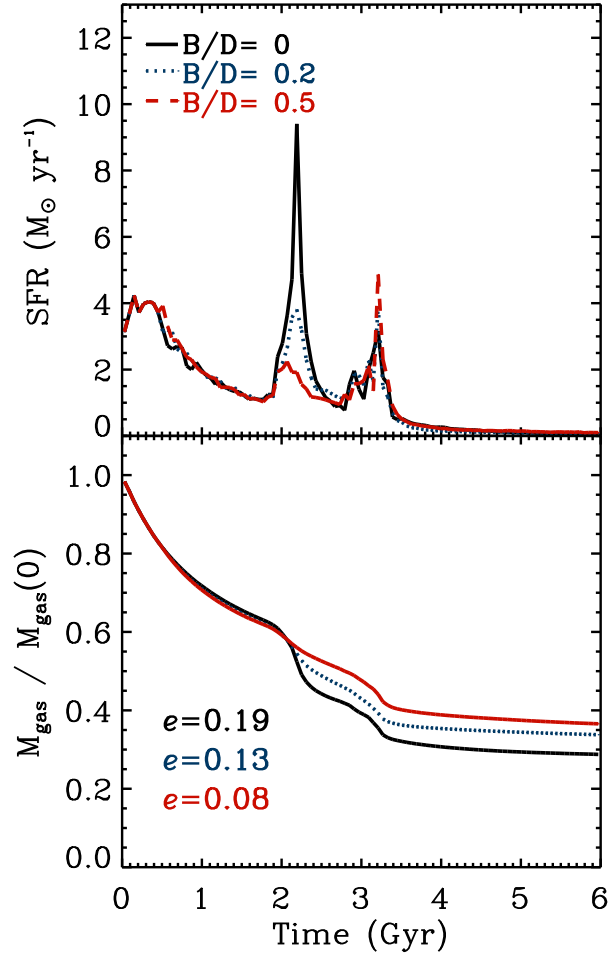


Figure 20. Star formation during unequal mass interactions as a function of primary bulge mass. The interaction is similar to the fiducial G3G1, except the orbit is co-planar (0°) and has less angular momentum (see text) in order to produce the maximum starburst. All runs are performed with the the *n0med* feedback model.

increasing the primary’s gas fraction decreases the burst efficiency. In effect, the result is similar to that presented in §5.2 for the distribution of gas and follows from a similar cause — the increased gas consumption in the isolated primary. In both scenarios, the initial disk converts a large fraction its gas into stars regardless of whether the interaction occurs or not.

6 DISCUSSION

In this paper we perform a series of numerical simulations that follow the interaction and merger of binary galaxies with various mass ratios. Our analysis quantifies the starbursts that result from the tidal forces that attend the merger. As expected, mergers between galaxies with nearly equal mass generate the largest tidal forces, and therefore produce the most intense bursts of star formation. Mergers between galaxies with a large mass ratio produce relatively little, if any, enhancement in star formation above quiescent

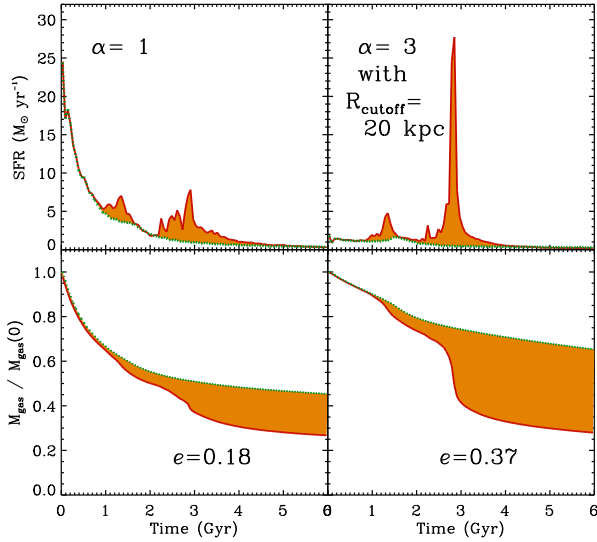


Figure 21. Star formation history and gas consumption for the fiducial G3G2 merger and two similar interactions where the primary G3 galaxy has a larger gas fraction. As with Figure 14, the difference between the merger and isolated evolution is shaded for clarity. The burst efficiency is displayed in the lower-right of the bottom panel. We note that the simulation here were run with the *n2med* feedback model while the mergers shown in Figure 14 employed the *n0med* model.

evolution, yielding a correlation between merger-driven star formation and decreasing merging galaxy mass ratio.

To quantify the relationship between merging galaxy mass ratio and merger-driven starburst, we introduce the burst efficiency (Eq. 5) as the fraction of gas that is converted into stars during the interaction which does not occur if the galaxies are evolved in isolation. The burst efficiency is demonstrated to be robust to uncertainties in the feedback parameterization unlike the strength or duration of the starburst.

While the burst efficiency resulting from collisions between galaxies of equivalent mass is relatively insensitive to the details of the merging event such as the orbit, the galaxy orientation, and the properties of the merging galaxies (Mihos & Hernquist 1996; Springel 2000; Cox 2004), this is not the case when the participating galaxies are unequal in mass.

By performing a large number of additional merger simulations, we have quantified the effects of merging orbit and orientation, as well as properties of the progenitor disk. We find that close passage, co-planar orbits produce the most significant bursts of star formation, consistent with the expectations of the tidally induced origin for the starbursts. We also find that the structure of the progenitor disk strongly influences the merger-driven star formation. In particular, the presence of a centrally-concentrated stellar bulge stabilizes the disk and suppresses merger-driven star formation. The distribution and mass of the gaseous disk also influences the starburst. In general, increasing the amount of gas at densities above ρ_{crit} , the threshold density for star formation to commence, decreases the burst efficiency.

These results lead us to conclude the following two facts about merger-driven starburst during an unequal mass

galaxy merger: (1) significant starbursts occur for only specialized scenarios, e.g., close passage, co-planar orientations, when the primary disk does not contain a bulge, and (2) even in this extreme scenario, the burst efficiency is still only $\lesssim 0.25$, i.e., a single unequal mass merger does not convert a large fraction of gas into stars.

6.1 Comparison to Previous Simulations

Our work is closely related to, and consistent with, a number of prior studies of the gas dynamics during the interaction and merger of unequal mass galaxies (e.g., Hernquist 1989; Mihos & Hernquist 1994a; Hernquist & Mihos 1995). While all work performed to date demonstrates that minor mergers can induce radial inflows of gas that result in periods of enhanced star formation, our models typically result in smaller burst efficiencies (see §4.3.1 and §4.4.1) owing to three key differences in the studies.

First, as shown in Cox et al. (2006) using simulations of major mergers, the more complex treatment of the interstellar medium produces more hot gas, and suppresses star formation. In particular, relaxing the isothermal gas assumption commonly employed in the work of Mihos & Hernquist, including the “conservative-entropy” (Springel & Hernquist 2002) version of SPH, and the more efficient feedback models of Cox et al. (2006) all serve to suppress the merger-induced starburst, and lower the burst efficiency.

Second, the set of simulations employed by Mihos & Hernquist (1994a) and Hernquist & Mihos (1995) followed satellite galaxies that were initially placed on a circular orbit. In contrast, we follow parabolic orbits which are motivated by cosmological expectations (see §4). These more energetic orbits lead to less direct coupling between the orbital angular momentum of the satellite and the disk of the primary, and therefore are less conducive to an intense inflow of disk gas.

Lastly, as noted in §5.3 and in Cox et al. (2006), the star formation model employed by Mihos & Hernquist is less efficient than current observations suggest (e.g., Kennicutt 1998). The primary result of this assumption is that the quiescent galaxy consumes much less gas when evolved in isolation and the merger burst efficiency is overestimated.

While there are additional differences between the galaxy models employed by these previous studies, namely they use less massive and less concentrated dark matter halos, and the baryonic components are not as faithful a representation of observed galaxies in the local Universe, the tests performed in §5 indicate that these differences play a secondary role to the three items outlined above. Even when we modified every possible parameter to maximize the burst efficiency, our value was still only one-third as large as the previous results.

6.2 Comparison to Observations

While observational studies have already established a clear link between star formation and galaxy interactions (as measured by close pairs or morphology, e.g., Larson & Tinsley 1978; Joseph & Wright 1985; Kennicutt et al. 1987; Barton Gillespie et al. 2003; Lambas et al. 2003; Nikolic et al. 2004), only recently

has it been possible to specifically address whether or not this correlation holds when the close galaxy pairs have rather disparate luminosities. In particular, Woods et al. (2006) reported no correlation between star formation (as measured by $H\alpha$) and close galaxy pairs in the CfA2 Redshift Survey when the magnitude difference is greater than 2, and a more recent study using a larger sample from SDSS found that the satellite galaxy indeed shows enhanced star formation while the primary did not (Woods & Geller 2007).

Assuming that luminosity traces mass (and modulo any systematic affects owing to merger-driven star formation), the studies by Woods et al. imply that there is no observational evidence for induced star formation in the primary galaxy when the merger mass ratio is greater than $\sim 6:1$, while the satellite is more likely to experience a starburst. Taken at face value, our results naturally recover this observed trend. Our merger models produce little, if any, globally enhanced star formation for merger mass ratios below 5:1, and when they do, it requires very specific circumstances (bulgeless primary, co-planar, close-passage orbit). It is also intriguing that Figure 8 hints that the satellite is much more susceptible to enhanced star-formation during the interaction, which also seems consistent with the observations.

In contrast to the statistical studies, there are a multitude of observations that suggest that individual systems are currently undergoing minor merger induced episodes of star formation (see the list in §1). To determine whether these specific galaxies are consistent with the statistical studies requires more extensive modeling of individual systems, as has been performed in a few cases already (see, e.g., Mihos & Bothun 1997; Laine & Heller 1999; Salo & Laurikainen 2000). It is possible that many of these systems have unique satellite orbits, or that the effects of multiple minor mergers which occur simultaneously is more dramatic than the binary mergers that we have followed here. Models of individual galaxies, and their direct comparison to observations across many wavebands may also yield important constraints to the star formation and feedback models.

6.3 Implications for Dwarf Galaxies

While the focus of our analysis has been on the global properties of merger-driven star formation, Figure 8 clearly demonstrates that the star formation history of the satellite galaxy can be enhanced far more dramatically than that of the primary galaxy (which dominates the global star formation). Such a scenario appears to be observed in the large sample of SDSS galaxies studied by Woods & Geller (2007) and also in the nearby Universe, e.g., both M82 and NGC 3077 are currently experiencing periods of intense star formation after recent close passages to M81 (Yun et al. 1994; Walter et al. 2002; Ott et al. 2003). These tidally-induced episodes of star formation may also have implications for the detection of satellite galaxies and the inferred cosmological merger rate (see, e.g., Berrier et al. 2006).

6.4 The Mass-Dependence of Star Formation

One interesting feature present in Figure 15 is the systematic dependence of $e_{1:1}$, the burst efficiency for an equal-

mass major merger, on primary galaxy mass. Specifically, the burst efficiency is 0.46 for the G3G3 major merger and steadily increases to 0.61 for the G0G0 major merger.

The increasing burst efficiency $e_{1:1}$ with decreasing system mass is a direct byproduct of systematic changes in the merger-induced star formation compared to that in the isolated disks. One possibility for this trend is the systematic increase in gas fraction with decreasing galaxy mass that is assumed for our galaxy models. However, the results of §5.4 suggest that increasing the gas fraction actually decreases the burst efficiency.

A more likely scenario is that the density-dependent description of star formation, including the explicit density threshold ρ_{crit} for star formation to commence, is producing the large variation in burst efficiency with mass. In particular, Figure 2 shows that the quiescent star formation spans three orders of magnitude from G3 ($\sim 1 \text{ M}_\odot \text{ yr}^{-1}$) to G0 ($\sim 10^{-3} \text{ M}_\odot \text{ yr}^{-1}$), while the peak star formation during the major mergers are much more comparable (G3G3 $\sim 25 \text{ M}_\odot \text{ yr}^{-1}$ and G0G0 $\sim 3 \text{ M}_\odot \text{ yr}^{-1}$). The significant increase in merger-induced star formation compared to quiescent levels was noted in §4.3 which determined that the G3G3 merger enhances star formation by a mere order of magnitude while the G0G0 merger enhances star formation by a whopping three orders of magnitude.

More work is required to determine the precise nature of the mass-dependence of star formation and how this trend depends upon uncertainties associated with our implementation of star formation. Moreover, a systematic comparison to the observed relationship between specific star formation rate and stellar mass, i.e. downsizing (Cowie et al. 1996; Brinchmann & Ellis 2000; Kauffmann et al. 2003), may elucidate the physical mechanisms responsible.

6.5 Input for Future Studies

Quantifying the merger-driven star formation as a function of merger mass ratio is useful for a variety of further studies. In particular, semi-analytic models of galaxy formation (SAMs) often find that merger-driven star formation is necessary to reproduce the luminosity function and number counts of Lyman-break galaxies (Somerville et al. 2001) and sub-millimeter galaxies (Guiderdoni et al. 1998; Baugh et al. 2005). To this end, we have followed the methodology of Somerville et al. (2001) and introduced the burst efficiency (see §4.4.1 and Eq. 5) in order to parameterize the star formation enhancement that occurs during galaxy interactions as a function of participant mass ratio.

In Table 3 we list the best fit parameters to Eq.5 for all models explored in this paper, including the fiducial series of runs (§4.4.1), and all additional models (orbits in §5.1, bulge-to-disk ratios in §5.3, and gas fractions of the progenitor disk in §5.4) that use the G3 primary galaxy. A quick inspection of Table 3 indicates that the parameter $e_{1:1}$, which normalizes Eq. 5 to the burst efficiency of a major merger, changes relatively little across this wide range of tests, although it may depend on galaxy mass (see the discussion of §6.4). On the other hand, the parameter γ , which determines the mass ratio scaling, has a significant dependence on orbital inclination and bulge-to-disk ratio, a mild dependence on the orbital angular momentum, and a negligible dependence upon gas fraction.

Table 3. Compilation of best fit burst efficiency (see §4.4.1 and Eq. 5) parameters for various sets of simulations employed in this paper. All simulations analyzed for these fits used the *n2med* feedback model.

Section	$e_{1:1}$	γ	Comment
4.4.1	0.55	0.69	fiducial series
5.1	0.49	0.94	$R_{\text{peri}} = 1.7$ kpc
5.1	0.49	0.82	$R_{\text{peri}} = 3.4$ kpc
5.1	0.49	0.66	$R_{\text{peri}} = 6.8$ kpc
5.1	0.50	0.74	$R_{\text{peri}} = 13.6$ kpc
5.1	0.51	0.87	$R_{\text{peri}} = 27.2$ kpc
5.1	0.50	0.96	$R_{\text{peri}} = 64.4$ kpc
5.1	0.50	0.47	0°
5.1	0.50	0.74	30°
5.1	0.50	0.96	60°
5.1	0.49	1.25	90°
5.1	0.49	0.99	150°
5.1	0.51	0.73	180°
5.3	0.50	0.61	$B/D = 0.0$
5.3	0.50	0.74	$B/D = 0.2$
5.3	0.50	1.02	$B/D = 0.5$
5.4	0.50	0.74	$f = 0.20$
5.4	0.49	0.74	$f = 0.50$
5.4	0.44	0.72	$f = 0.78$

While the burst efficiency is a useful quantification of the star-formation induced by a galaxy merger, a better understanding of the star-formation timescale is necessary to completely describe merger-induced star formation. Unfortunately, as shown in §4.3.3, uncertainties in the feedback model do not permit an unambiguous characterization of the star-formation timescale. There is hope, however, that better constraints can be placed on the feedback model through more detailed modeling of individual systems or by comparison to the observed distribution of star formation rates.

Finally, we emphasize that the accretion events followed in this study drive structural evolution which is also an interesting and relevant input parameter to future studies of galaxy formation and evolution. In particular, the morphology of the merger remnants (see Figs. 3–6) suggests that the stellar and gaseous components react differently to the dynamical perturbation and that the remnant appears to be a systematically earlier Hubble type than the original disk. This is also consistent with the surface density profile shown in Figure 9, which shows an excess of mass at small radii indicative of the formation of a stellar bulge.

6.6 Other Considerations

As a final comment, we note that the present simulations lack several physical processes that may play a role in the results we have presented. First, we have not included the recycling of gas from stellar winds and supernovae, an omission that would increase the gas fraction as a function of time. Another process that may increase the gas content on long timescales is the accretion of gas from the cosmological growth of structure. While we eventually intend to incor-

porate these effects into our modeling (as has been done by several authors already, see, e.g., Tornatore et al. 2004; Scannapieco et al. 2005; Stinson et al. 2006), the relatively small difference ($\sim 15\%$) in the burst efficiency for runs of different initial gas fractions (see §5.4) supports the notion that this omission has a relatively minor effect on the star formation that results from a single merger. However, for the long-term evolution, and for the absolute star-formation rate, these effects are likely to be important.

It should also be pointed out that our galaxy models are calibrated to match low redshift observations of disk galaxies. While we have surveyed a small portion of the parameter space that might correspond to properties of disks at higher redshift, e.g., higher gas fractions and more compact initial disks, and therefore have some indication of the changes that may occur, future studies will need to investigate these dependencies in more depth.

We have also not included accreting black holes and their associated feedback into the models presented here. Recent work has shown that these processes may play a significant role during major mergers, resulting in the formation of quasars (Hopkins et al. 2006), and leading to remnants that reside on the $M_{\text{BH}} - \sigma$ relation (Di Matteo et al. 2005; Springel et al. 2005b; Robertson et al. 2006) and have the colors (Springel et al. 2005a) and other properties (Cox et al. 2006; Robertson et al. 2006) appropriate for present day elliptical galaxies. While the minor interactions we discuss here are a likely fueling mechanism for many forms of nuclear activity (see, e.g., Hopkins & Hernquist 2006), because significant black hole growth requires large quantities of gas (approximately the entire content of the initial disks) to be driven to the galactic center, it is likely that black hole growth and feedback play a relatively minor part during most of the unequal mass interactions we follow here. Of course, the existence of a correlation between the black hole mass and the bulge mass (see, e.g., Magorrian et al. 1998) suggests that at the very minimum the black hole imparts enough feedback to regulate its own growth.

ACKNOWLEDGMENTS

We thank Gurtina Besla, Suvendra Dutta, Lars Hernquist, Phil Hopkins, Jennifer Lotz, Greg Novak, Brant Robertson, and Josh Younger for helpful discussions, and Eric Bell for providing his data in electronic form. This research used the Beowulf UpsAnd at UCSC and computational resources at the National Energy Research Scientific Computing Center (NERSC), which is supported by the Office of Science of the US Department of Energy. TJC, AD, and JRP acknowledge support from NASA and NSF grants at UCSC. PJ was supported by a UC/LLNL cooperative grant from IGPP to Wil van Breugel, and by program numbers HST-AR-10678 and HST-AR-10958, provided by NASA through grants from the Space Telescope Science Institute, which is operated by the Association of Universities for Research in Astronomy, Incorporated, under NASA contract NAS5-26555.

REFERENCES

Aguerre J. A. L., Balcells M., Peletier R. F., 2001, *A&A*,

- 367, 428
 Alam S. M. K., Bullock J. S., Weinberg D. H., 2002, *ApJ*, 572, 34
 Barnes J. E., 2004, *MNRAS*, 350, 798
 Barnes J. E., Hernquist L., 1992, *ARA&A*, 30, 705
 Barnes J. E., Hernquist L. E., 1991, *ApJL*, 370, L65
 Barton E. J., Arnold J. A., Zentner A. R., Bullock J. S., Wechsler R. H., 2007, submitted to *ApJ*
 Barton E. J., Geller M. J., Kenyon S. J., 2000, *ApJ*, 530, 660
 Barton Gillespie E., Geller M. J., Kenyon S. J., 2003, *ApJ*, 582, 668
 Baugh C. M., Lacey C. G., Frenk C. S., Granato G. L., Silva L., Bressan A., Benson A. J., Cole S., 2005, *MNRAS*, 356, 1191
 Bell E. F., de Jong R. S., 2001, *ApJ*, 550, 212
 Bell E. F., McIntosh D. H., Katz N., Weinberg M. D., 2003, *ApJL*, 585, L117
 Benson A. J., 2005, *MNRAS*, 358, 551
 Benson A. J., Lacey C. G., Frenk C. S., Baugh C. M., Cole S., 2004, *MNRAS*, 351, 1215
 Berrier J. C., Bullock J. S., Barton E. J., Guenther H. D., Zentner A. R., Wechsler R. H., 2006, *ApJ*, 652, 56
 Borne K. D., Bushouse H., Lucas R. A., Colina L., 2000, *ApJL*, 529, L77
 Bournaud F., Combes F., Jog C. J., 2004, *A&A*, 418, L27
 Bournaud F., Jog C. J., Combes F., 2005, *A&A*, 437, 69
 Boylan-Kolchin M., Ma C.-P., 2007, *MNRAS*, 374, 1227
 Brinchmann J., Ellis R. S., 2000, *ApJL*, 536, L77
 Broeils A. H., van Woerden H., 1994, *A&AS*, 107, 129
 Bullock J. S., Johnston K. V., 2005, *ApJ*, 635, 931
 Bullock J. S., Kolatt T. S., Sigad Y., Somerville R. S., Kravtsov A. V., Klypin A. A., Primack J. R., Dekel A., 2001, *MNRAS*, 321, 559
 Cortés J. R., Kenney J. D. P., Hardy E., 2006, *AJ*, 131, 747
 Covington M., Dekel A., Cox T. J., Primack J. R., Jonsson P., 2007, *MNRAS* submitted, 000, L0
 Cowie L. L., Songaila A., Hu E. M., Cohen J. G., 1996, *AJ*, 112, 839
 Cox T. J., 2004, PhD thesis, UC Santa Cruz, <http://physics.ucsc.edu/tj/work/thesis>
 Cox T. J., Di Matteo T., Hernquist L., Hopkins P. F., Robertson B., Springel V., 2006, *ApJ*, 643, 692
 Cox T. J., Dutta S., Di Matteo T., Hernquist L., Hopkins P. F., Robertson B., Springel V., 2006, *ApJ*, 650, 791
 Cox T. J., Jonsson P., Primack J. R., Somerville R. S., 2006, *MNRAS*, 373, 1013
 Cox T. J., Primack J., Jonsson P., Somerville R. S., 2004, *ApJL*, 607, L87
 Dalcanton J. J., Bernstein R. A., 2002, *AJ*, 124, 1328
 de Jong R. S., 1996, *A&A*, 313, 45
 de Vaucouleurs G., 1977, in Tinsley B. M., Larson R. B., eds, *Evolution of Galaxies and Stellar Populations Qualitative and Quantitative Classifications of Galaxies..* pp 43–+
 Dekel A., Cox T. J., 2006, *MNRAS*, 370, 1445
 di Matteo P., Combes F., Melchior A.-L., Semelin B., 2007, *A&A*, 468, 61
 Di Matteo T., Springel V., Hernquist L., 2005, *Nature*, 433, 604
 Eliche-Moral M. C., Balcells M., Aguerri J. A. L., González-García A. C., 2006, *A&A*, 457, 91
 Ellison S. L., Patton D. R., Simard L., McConnachie A. W., 2007, submitted to *ApJ*
 Font A. S., Navarro J. F., Stadel J., Quinn T., 2001, *ApJL*, 563, L1
 Förster Schreiber N. M., Genzel R., Lutz D., Sternberg A., 2003, *ApJ*, 599, 193
 Geha M., Blanton M. R., Masjedi M., West A. A., 2006, *ApJ*, 653, 240
 Geller M. J., Kenyon S. J., Barton E. J., Jarrett T. H., Kewley L. J., 2006, *AJ*, 132, 2243
 Guiderdoni B., Hivon E., Bouchet F. R., Maffei B., 1998, *MNRAS*, 295, 877
 Harker J. J., Schiavon R. P., Weiner B. J., Faber S. M., 2006, *ApJL*, 647, L103
 Helmi A., White S. D. M., 2001, *MNRAS*, 323, 529
 Hernquist L., 1989, *Nature*, 340, 687
 Hernquist L., 1990, *ApJ*, 356, 359
 Hernquist L., 1992, *ApJ*, 400, 460
 Hernquist L., 1993a, *ApJS*, 86, 389
 Hernquist L., 1993b, *ApJ*, 409, 548
 Hernquist L., Mihos J. C., 1995, *ApJ*, 448, 41
 Hopkins P. F., Hernquist L., 2006, *ApJS*, 166, 1
 Hopkins P. F., Hernquist L., Cox T. J., Di Matteo T., Robertson B., Springel V., 2006, *ApJS*, 163, 1
 Hopkins P. F., Somerville R. S., Hernquist L., Cox T. J., Robertson B., Li Y., 2006, *ApJ*, 652, 864
 Huang S., Carlberg R. G., 1997, *ApJ*, 480, 503
 Hubble E. P., 1926, *ApJ*, 64, 321
 Ibata R., Irwin M., Lewis G., Ferguson A. M. N., Tanvir N., 2001, *Nature*, 412, 49
 Johnston K. V., Zhao H., Spergel D. N., Hernquist L., 1999, *ApJL*, 512, L109
 Jonsson P., 2004, PhD thesis, UC Santa Cruz, <http://sunrise.familjenjonsson.org/thesis>
 Jonsson P., 2006, *MNRAS*, 372, 2
 Jonsson P., Cox T. J., Primack J. R., Somerville R. S., 2006, *ApJ*, 637, 255
 Joseph R. D., Wright G. S., 1985, *MNRAS*, 214, 87
 Kapferer W., Knapp A., Schindler S., Kimeswenger S., van Kampen E., 2005, *A&A*, 438, 87
 Katz N., Weinberg D. H., Hernquist L., 1996, *ApJS*, 105, 19
 Kauffmann G., Heckman T. M., White S. D. M., Charlot S., Tremonti C., Peng E. W., Seibert M., Brinkmann J., Nichol R. C., SubbaRao M., York D., 2003, *MNRAS*, 341, 54
 Kay S. T., Pearce F. R., Frenk C. S., Jenkins A., 2002, *MNRAS*, 330, 113
 Kennicutt R. C., 1998, *ApJ*, 498, 541
 Kennicutt R. C., Roettiger K. A., Keel W. C., van der Hulst J. M., Hummel E., 1987, *AJ*, 93, 1011
 Khochfar S., Burkert A., 2006, *A&A*, 445, 403
 Knapen J. H., Whyte L. F., de Blok W. J. G., van der Hulst J. M., 2004, *A&A*, 423, 481
 Kormendy J., Fischer D. B., Cornell M. E., Bender R., 2007, submitted to *ApJ*
 Lacey C., Cole S., 1993, *MNRAS*, 262, 627
 Laine S., Heller C. H., 1999, *MNRAS*, 308, 557
 Lambas D. G., Tissera P. B., Alonso M. S., Coldwell G., 2003, *MNRAS*, 346, 1189

- Larson R. B., Tinsley B. M., 1978, *ApJ*, 219, 46
- Lin L., Koo D. C., Weiner B. J., Chiueh T., Coil A. L., Lotz J., Conselice C. J., Willner S. P., Smith H. A., Guhathakurta P., Huang J.-S., Le Floch E., Noeske K. G., Willmer C. N. A., Cooper M. C., Phillips A. C., 2007, *ApJL*, 660, L51
- Magorrian J., Tremaine S., Richstone D., Bender R., Bower G., Dressler A., Faber S. M., Gebhardt K., Green R., Grillmair C., Kormendy J., Lauer T., 1998, *AJ*, 115, 2285
- Maller A. H., Katz N., Kereš D., Davé R., Weinberg D. H., 2006, *ApJ*, 647, 763
- Mayer L., Moore B., Quinn T., Governato F., Stadel J., 2002, *MNRAS*, 336, 119
- Mazzuca L. M., Sarzi M., Knapen J. H., Veilleux S., Swaters R., 2006, *ApJL*, 649, L79
- Mihos J. C., Bothun G. D., 1997, *ApJ*, 481, 741
- Mihos J. C., Hernquist L., 1994a, *ApJL*, 425, L13
- Mihos J. C., Hernquist L., 1994b, *ApJL*, 431, L9
- Mihos J. C., Hernquist L., 1996, *ApJ*, 464, 641
- Mo H. J., Mao S., White S. D. M., 1998, *MNRAS*, 295, 319
- Naab T., Burkert A., 2003, *ApJ*, 597, 893
- Navarro J. F., Frenk C. S., White S. D. M., 1996, *ApJ*, 462, 563
- Navarro J. F., Helmi A., Freeman K. C., 2004, *ApJL*, 601, L43
- Nikolic B., Cullen H., Alexander P., 2004, *MNRAS*, 355, 874
- Noeske K. G., al. e., 2007, *ApJL*, 660, L43
- Novak G. S., Cox T. J., Primack J. R., Jonsson P., Dekel A., 2006, *ApJL*, 646, L9
- Ott J., Martin C. L., Walter F., 2003, *ApJ*, 594, 776
- Quinn P. J., Goodman J., 1986, *ApJ*, 309, 472
- Quinn P. J., Hernquist L., Fullagar D. P., 1993, *ApJ*, 403, 74
- Robertson B., Cox T. J., Hernquist L., Franx M., Hopkins P. F., Martini P., Springel V., 2006, *ApJ*, 641, 21
- Robertson B., Hernquist L., Cox T. J., Di Matteo T., Hopkins P. F., Martini P., Springel V., 2006, *ApJ*, 641, 90
- Rocha M., Jonsson P., Primack J. R., Cox T. J., 2007, *MNRAS*, submitted (astro-ph/0702513), 000, 000
- Rothberg B., Joseph R. D., 2004, *AJ*, 128, 2098
- Salo H., Laurikainen E., 2000, *MNRAS*, 319, 377
- Sandage A., 1975, *Classification and Stellar Content of Galaxies Obtained from Direct Photography. Galaxies and the Universe*, pp 1–+
- Sanders D. B., Mirabel I. F., 1996, *ARA&A*, 34, 749
- Scannapieco C., Tissera P. B., White S. D. M., Springel V., 2005, *MNRAS*, 364, 552
- Schweizer F., 1998, in Friedli D., Martinet L., Pfenniger D., eds, *Saas-Fee Advanced Course 26: Galaxies: Interactions and Induced Star Formation Galaxies: Interactions and Induced Star Formation*
- Shen S., Mo H. J., White S. D. M., Blanton M. R., Kauffmann G., Voges W., Brinkmann J., Csabai I., 2003, *MNRAS*, 343, 978
- Smith B. J., Struck C., Hancock M., Appleton P. N., Charmandaris V., Reach W. T., 2007, *AJ*, 133, 791
- Smith D. A., Neff S. G., Bothun G. D., Fanelli M. N., Offenberg J. D., Waller W. H., Bohlin R. C., O’Connell R. W., Roberts M. S., Smith A. M., Stecher T. P., 1996, *ApJL*, 473, L21+
- Sol Alonso M., Lambas D. G., Tissera P., Coldwell G., 2006, *MNRAS*, 367, 1029
- Somerville R. S., Primack J. R., 1999, *MNRAS*, 310, 1087
- Somerville R. S., Primack J. R., Faber S. M., 2001, *MNRAS*, 320, 504
- Springel V., 2000, *MNRAS*, 312, 859
- Springel V., Di Matteo T., Hernquist L., 2005a, *ApJL*, 620, L79
- Springel V., Di Matteo T., Hernquist L., 2005b, *MNRAS*, 361, 776
- Springel V., Hernquist L., 2002, *MNRAS*, 333, 649
- Springel V., Hernquist L., 2003, *MNRAS*, 339, 289
- Springel V., White S. D. M., 1999, *MNRAS*, 307, 162
- Springel V., Yoshida N., White S. D. M., 2001, *New Astronomy*, 6, 79
- Stinson G., Seth A., Katz N., Wadsley J., Governato F., Quinn T., 2006, *MNRAS*, 373, 1074
- Struck C., 1997, *ApJS*, 113, 269
- Struck C., 2006, *Galaxy Collisions - Dawn of a New Era. Astrophysics Update 2*, pp 115–+
- Thacker R. J., Couchman H. M. P., 2000, *ApJ*, 545, 728
- Toomre A., 1977, in *Evolution of Galaxies and Stellar Populations Mergers and Some Consequences*. p. p.401
- Tornatore L., Borgani S., Matteucci F., Recchi S., Tozzi P., 2004, *MNRAS*, 349, L19
- Toth G., Ostriker J. P., 1992, *ApJ*, 389, 5
- van den Bergh S., 1960, *ApJ*, 131, 215
- Velazquez H., White S. D. M., 1999, *MNRAS*, 304, 254
- Vitvitska M., Klypin A. A., Kravtsov A. V., Wechsler R. H., Primack J. R., Bullock J. S., 2002, *ApJ*, 581, 799
- Walker I. R., Mihos J. C., Hernquist L., 1996, *ApJ*, 460, 121
- Walter F., Weiss A., Martin C., Scoville N., 2002, *AJ*, 123, 225
- Wechsler R. H., Bullock J. S., Primack J. R., Kravtsov A. V., Dekel A., 2002, *ApJ*, 568, 52
- Woods D. F., Geller M. J., 2007, *AJ*, 134, 527
- Woods D. F., Geller M. J., Barton E. J., 2006, *AJ*, 132, 197
- Younger J. D., Cox T. J., Seth A. C., Hernquist L., 2007, *ApJaccepted* (astro-ph/0707.4481), 707
- Yun M. S., Ho P. T. P., Lo K. Y., 1994, *Nature*, 372, 530
- Zentner A. R., Berlind A. A., Bullock J. S., Kravtsov A. V., Wechsler R. H., 2005, *ApJ*, 624, 505